Institut für Angewandte Physik
der Universität Bonn

Wegelerstraße 8
53115 Bonn

Resolved Raman sideband cooling in a doughnut-shaped optical trap

von
Sebastian Hild

Masterarbeit in Physik

angefertigt im
Institut für Angewandte Physik

vorgelegt der
Mathematisch-Naturwissenschaftlichen Fakultät
der Rheinischen Friedrich-Wilhemls-Universität
Bonn

Oktober 2011

1. Gutachter: Prof. Dr. D. Meschede
2. Gutachter: Prof. Dr. A. Widera

Contents

1 Introduction 1

2 Coherent cold collisions 3
  2.1 Theoretical considerations of cold collisions 3
  2.2 Expected cold collisions 7

3 Doughnut shaped optical dipole trap 11
  3.1 Present experimental setup 11
  3.2 Higher radial trapping frequency with the doughnut beam 13
    3.2.1 Laser system 17
    3.2.2 Spacial and spectral filtering 17
    3.2.3 Integration into the current setup 20
  3.3 Trap parameters 22
  3.4 First results 23

4 Resolved Raman sideband cooling 27
  4.1 Sideband transitions in an optical lattice 27
    4.1.1 Microwave-induced sidebands 29
    4.1.2 Two photon induced sidebands 30
  4.2 Theory of stimulated Raman transitions 31
    4.2.1 Raman transitions in an ideal three level system 31
    4.2.2 Magnetic substates of the hyperfine structure 32
  4.3 Cooling scheme 33
  4.4 Optical phase lock loop 36
  4.5 Experimental setup 38
    4.5.1 Phase frequency detector 40
  4.6 Characterization of the OPLL 42
    4.6.1 Quadrature measurement 42
    4.6.2 Beat signal 42
  4.7 Measurements 44
    4.7.1 Rabi oscillations 45
    4.7.2 Ramsey oscillations 48

5 Outlook 51

Bibliography 53

List of Figures 57

List of Tables 59

A Further calculation of the overlap integral 61

B Phase frequency discriminator circuit diagram 63

1 Introduction

During the last century, quantum mechanics has become one of the most important and successful theories in physics. The theory can explain many experimental results which were found in conflict with classical mechanics. Since then, many experiments have revealed fundamental quantum mechanical phenomena. Currently, scientific research moves from mere observation of these effects to their control and utilization. The shared goal is to construct quantum simulators or quantum computers. The basis for calculations of a quantum computer is the so called quantum bit or short qubit. It consists of two states often called $|0\rangle$ and $|1\rangle$. In contrast to a classical bit which can be either in state $|0\rangle$ or $|1\rangle$, the qubit can also be in any quantum mechanical superposition of these two states. Operations on these qubits are done by quantum mechanical analogs to classical registers. Quantum algorithms require the capability to entangle qubits in quantum registers.

There exist situations where it is already known that quantum computers could be faster than classical computers. Today, the factorization algorithm of Shor is one of the most famous examples [1]. Five general criteria which a candidate for a quantum computer implementation must fulfill were published by DiVincenzo [2]. These criteria govern the scalability and the universality of the system. Although theoretical concepts exist on how a quantum computer could be realized [3] it is very challenging to build a flexible system with many qubits.

First experiments where done with nuclear magnetic resonance techniques [4], but these systems lack scalability. Cold trapped ions are nowadays employed for ultra precise time keeping and to realize different quantum logic gates [5]. In a recent experiment it was achieved to entangle 14 ions [6]. In solid state physics Josephson junctions are under consideration to build quantum computers [7].

Another promising alternative are neutral atoms in optical traps. During the past 20 years, lasers made it possible to cool large an ensemble of neutral atoms down to a Bose-Einstein Condensate [8] and also to study single trapped neutral atoms precisely. As neutral atoms couple very weakly to their environment they are advantageous to carry out experiments without disturbances. The interaction between two atoms needed to entangle these can be realized by photons in high finesse cavities. Two Rydberg atoms can also be entangled using the Rydberg blockade [9]. An alternative approach to realize a controlled interaction could be via controlled coherent cold collisions [10]. So far, this has been realized with Bose-Einstein condensates, without direct control of single qubits [11].

The system under consideration in this master thesis adopts the so-called "bottom-up" approach, which consists in constructing the system atom by atom. It works with single Cesium (Cs) atoms in a state dependent optical lattice [12], with the two hyperfine ground-states $|F=4{,}m=4\rangle$ and $|F=3{,}m=3\rangle$, forming the single qubit. The system has been used to realize quantum walks [13] and a single atom interferometer. Realization of entanglement of two or more atoms could be achieved via cold coherent collisions.

Initialization of atoms in the motional ground-state is a prerequisite of this technique, and it is the main topic of my master thesis. It is proposed to cool the Cs atoms to their motional ground-state using resolved Raman side band cooling. Resolved Raman side band cooling has been realized for single trapped ions [14] as well as for Cs atoms in an optical lattice [15]. Raman lasers are also used as high precision tools to drive Rabi pulses in atom interferometers [16].

Resolved Raman side band cooling works only in the Lamb-Dicke regime, when the trapping frequencies are bigger than the recoil energy. Because the current trap configuration does not provide this, the trap frequencies have to be increased. Our plan to achieve this is to superimpose a hollow blue-detuned laser beam, also called doughnut beam [17], to our present 1D optical lattice. This already has been demonstrated for cold Rubidium atoms in a different application[18].

2 Coherent cold collisions

Detailed examinations of collisions have driven the development of our current understanding of physics. For example, Rutherford analyzed the scattering of α and β particles by matter to deduce the structure of atoms and today, scientists at the LHC study intensively the collision between two protons at very high energies. Collisions play an important role for the formation of Bose-Einstein condensates and thus detailed studies of collisions had to be made at very low energies before creating the first BEC [19]. Nowadays the collisions can be precisely tuned with Feshbach resonances [20].
Our apparatus will allow us to study interacting atoms from a privileged point of view: The ability to control the collision between just two cesium atoms will lead to a clear signal. The apparatus makes it possible to control the precise state of each atom as well as the interaction time between two atoms. The scattering length a_{sc} is the characteristic parameter describing scattering at very low energies. The collision process between two cesium atoms inside our trap can be calculated with the knowledge of this parameter. I will present estimates for the phase evolution in different cases matching the experimental conditions.

2.1 Theoretical considerations of cold collisions

I assume to have a spherical symmetric interaction potential with a short range interaction of radius R. Beyond R, the interaction strength can be neglected. This problem can be addressed in partial wave approximation [21]. For atoms with energy E and mass m only partial waves with momentum eigenvalues $l < R\sqrt{2mE}/\hbar$ acquire a significant collisional phase shift. This corresponds to the classical case that atoms with higher energy do not get close enough to interact with the potential due to their angular momentum [22]. In our situation, the energy of the atoms is very low and just the partial waves with $l = 0$ have to be taken into account. This case is also referred to as s-wave scattering. The scattering length a_{sc} as a single parameter describing the scattering process can be introduced in the limit of zero energy. The cross section σ of such a scattering process is then given as:

$$\sigma = 4\pi a_{sc}^2.$$

For my experimenters the states $|\downarrow\rangle = |F = 4, m_F = 4\rangle$ and $|\uparrow\rangle = |F = 3, m_F = 3\rangle$ of the Cs hyperfine ground-state manifold are under consideration. The scattering length has been measured for pair $|\downarrow\downarrow\rangle$ to be $a_{\downarrow\downarrow} \sim -2700 a_0$ where $a_0 = (4\pi\varepsilon_0\hbar^2)/(m_e e^2)$ is the Bohr radius. For the pair $|\uparrow\downarrow\rangle$ only ab-initio calculations have been done resulting in

$a_{\downarrow\uparrow} \sim 2500a_0$ [23].
For two atoms with momentum operator $p^{a,b}$ and position operator $x^{a,b}$ inside the potential wells $V^{a,b}$, respectively, the Hamiltonian

$$H = \sum_{\beta=a,b} \left[\frac{\left(p^\beta\right)^2}{2m} + V^\beta \left(x^\beta\right) \right] + u^{ab} \left(x^a - x^b\right). \tag{2.1}$$

is adequate to describe the system [10]. Here u^{ab} describes the interaction between both atoms and only depends on the distance between both atoms. The wave functions $\psi_{a,b}\left(x^{a,b}\right)$ of the atoms are overlapped in a controlled adiabatic manner for a given amount of time t and afterwards separated again in order to prevent each atom from changing its wave function. The two atom state would transform as:

$$\psi_a\left(x^a\right)\psi_b\left(x^b\right) = e^{i\phi}\psi_a\left(x^a\right)\psi_b\left(x^b\right) \tag{2.2}$$

and the phase ϕ of the state after the collision contains a contribution due to the interaction. The time dependent energy shift $\mathit{\Delta} E\left(t\right)$ of the two interacting atoms can be calculated using:

$$\mathit{\Delta} E\left(t\right) = \frac{4\pi a_{sc}\hbar^2}{m} \int d^3x \left|\psi_a\left(x^a\left(t\right)\right)\right|^2 \left|\psi_b\left(x^b\left(t\right)\right)\right|^2. \tag{2.3}$$

The contribution of this energy shift to the phase can than be evaluated as

$$\phi^{ab} = \frac{1}{\hbar} \int\limits_{-t/2}^{t/2} dt \mathit{\Delta} E\left(t\right). \tag{2.4}$$

For my estimations, I neglect the overlap process and assume that the overlap could be controlled such that the atoms interact with constant strength for a given time t. The phase accumulated simplifies to

$$\phi^{ab} = \frac{4\pi a_{sc}\hbar \cdot t}{m} \int dx \prod_{\beta=a,b} \left|\psi_\beta\left(x\right)\right|^2. \tag{2.5}$$

As being a global phase this interaction would not be noticeable. A sequence which allows to measure the phase is shown in Figure 2.1. At the beginning, both atoms are in state $|\uparrow\rangle$ at the lattice positions n and $n+2$ inside our state dependent lattice described in Section 3.1. The process can be analyzed with the two atom wavefunction $|\uparrow, n\rangle\,|\uparrow, n+2\rangle$.

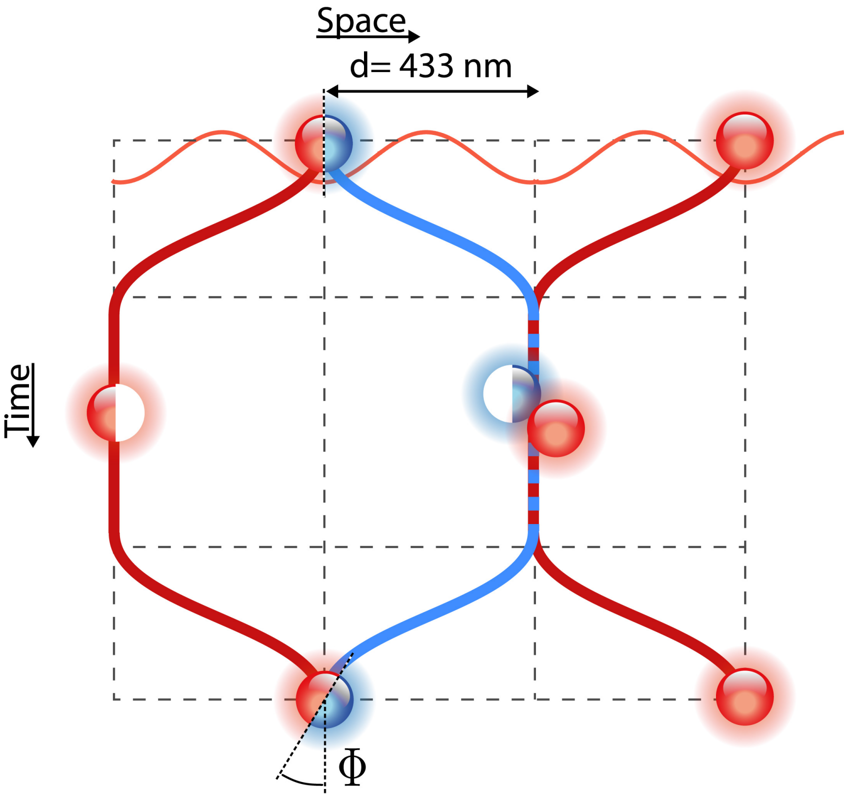

Figure 2.1: Sequence to measure the phase due to cold collision. The left atom is prepared in the superposition between $|\downarrow\rangle$ and $|\uparrow\rangle$, the right atom is prepared in $|\uparrow\rangle$. Using state-dependent transport, the two atoms are overlapped for a controllable time at the intermediate lattice site. Thereafter they are separated again and the phase of the left atom is read out using Ramsey like spin tomography.

During the sequence the wavefunction evolves as follows:

$$\begin{array}{ll}
|\uparrow, n\rangle\,|\uparrow, n+2\rangle & \text{initial state} \\
\frac{1}{\sqrt{2}}\left(|\uparrow, n\rangle + |\downarrow, n\rangle\right)|\uparrow, n+2\rangle & \frac{\pi}{2}\text{ pulse for atom in state } n \\
\frac{1}{\sqrt{2}}\left(|\uparrow, n-1\rangle + |\downarrow, n+1\rangle\right)|\uparrow, n+1\rangle & \text{state-dependent transport} \\
\frac{1}{\sqrt{2}}\left(|\uparrow, n-1\rangle + e^{i\phi^{\uparrow\downarrow}}\,|\downarrow, n+1\rangle\right)|\uparrow, n+1\rangle & \text{interaction} \\
\frac{1}{\sqrt{2}}\left(|\uparrow, n\rangle + e^{i\phi^{\uparrow\downarrow}}\,|\downarrow, n\rangle\right)|\uparrow, n+2\rangle & \text{state-dependent transport} \\
\frac{1}{2}\left(|\uparrow, n\rangle + |\downarrow, n\rangle\right)|\uparrow, n+2\rangle + e^{i\phi^{\uparrow\downarrow}}\frac{1}{2}\left(|\uparrow, n\rangle - |\downarrow, n\rangle\right)|\uparrow, n+2\rangle & \frac{\pi}{2}\text{ pulse for atom in state } n \\
e^{i\phi^{\uparrow\downarrow}}\left(\cos\left(\phi^{\uparrow\downarrow}\right)|\uparrow, n\rangle + \sin\left(\phi^{\uparrow\downarrow}\right)|\downarrow, n\rangle\right)|\uparrow, n+2\rangle & \text{rewritten}
\end{array}$$

At the end of the sequence, the population in state $|\uparrow\rangle$ can be read out using the selective push-out technique explained in Section 3.1. The provability $P(t)$ to detect atoms in state $|\uparrow\rangle|\uparrow\rangle$ is:

$$P(t) = \left|\langle\uparrow|\langle\uparrow| e^{i\phi^{\uparrow\downarrow}} \left(\cos\left(\phi^{\uparrow\downarrow}\right)|\uparrow, n\rangle + \sin\left(\phi^{\uparrow\downarrow}\right)|\downarrow, n\rangle\right)|\uparrow, n+2\rangle\right|^2 \tag{2.6}$$

$$= \cos^2\left(\phi^{\uparrow\downarrow}\right) \tag{2.7}$$

$$= \cos^2\left(\frac{4\pi a_{\uparrow\downarrow}\hbar\cdot t}{m}\int d^3x\,|\psi_a(x)|^2\,|\psi_b(x)|^2\right) \tag{2.8}$$

During the interaction, the two atoms occupy the same lattice site. The trapping potential at each lattice site can be approximated to be a 3D anisotropic harmonic trap with trapping frequency $\omega_\perp$ for the two axes perpendicular to the lattice (radial direction) and $\omega_\|$ for the longitudinal axis (axial direction). Rewriting the integral in Equation 2.5 in scale invariant variables points out the dependence on the trap frequencies and vibrational quantum numbers.

$$x_i = \sqrt{\frac{\hbar}{m\omega_i}}\tilde{x_i} \tag{2.9}$$

$$\psi(x) = \prod_{i=1,2,3}\left[\left(\frac{m\omega_i}{\pi\hbar}\right)^{\frac{1}{4}}\right]\tilde{\psi}(\tilde{x_i}) \tag{2.10}$$

$$\phi^{ab} = \frac{4\pi a_{sc}\hbar\cdot t}{m}\frac{m\omega_\perp}{\hbar}\sqrt{\frac{m\omega_\|}{\hbar}}\int d^3\tilde{x}\left|\tilde{\psi_a}(\tilde{x})\right|^2\left|\tilde{\psi_b}(\tilde{x})\right|^2 \tag{2.11}$$

As a first important result we can see that the phase accumulated during one collision is proportional to $\omega_\perp\sqrt{\omega_\|}$. Figure 2.2 shows the values for the integral $\int d\tilde{x}\prod_{\beta=a,b}\left|\tilde{\psi_\beta}(\tilde{x})\right|^2$ in one dimension for atom one in state n and atom two in state m. From this plot it becomes obvious that the phase rate deceases strongly if the atoms are not in the ground-state. The phase rate decreases even further if both atoms are in different motional states.

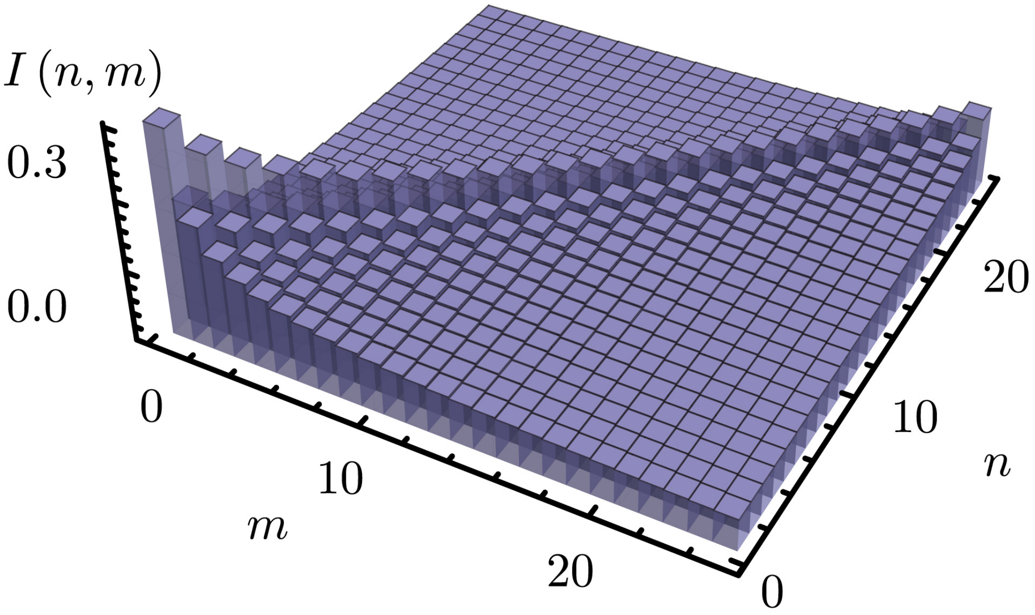

Figure 2.2: Integral $\int d\tilde{x} \prod_{\beta=a,b} \left|\tilde{\psi}_\beta(\tilde{x})\right|^2$ evaluated in one dimension for atom one in state n and atom two in state m.

2.2 Expected cold collisions

In the present setup atoms are cooled to the motional ground-state in axial direction with microwave sideband cooling described in Section 4.1. However, no cooling mechanism is applied to the radial directions, yet. The effect of not ground-state-cooled atoms can be simulated assuming a Boltzmann distribution over the perpendicular motional states. In the simulation of collisional physics I shall consider cold atoms with $\bar{n} \leq 5$ for each radial direction and in the ground-state for the axial direction. The Boltzmann distribution is truncated at $n_{max} = 25$ as the probability for $n > 25$ with $\bar{n} = 5$ is less than $0.9\,\%$. The interaction process has to be calculated for all combinations of the two vibrational states of the two atoms and weighted with the corresponding probability. The total amount of possible combinations is n_{max}^4. Using the symmetries of the system the amount of calculations can be reduced. Nevertheless, the computation time still scales with the fourth power of the maximal vibrational number. The current setup works with atoms with an average vibrational number around 200 and therefore simulation of this situation would require a long computation time, however, such high $\bar{n}$ are not necessary to simulate for the purpose of giving a prediction.

The simulations are done for both atoms in the $|\downarrow\rangle$ state as for this state the scattering length was measured. The axial trapping frequency is $\omega_{\|} = 115$ kHz [24] and the radial trapping frequency is $\omega_{\perp} = 20\,\text{kHz}$, 20-times larger than the trapping frequency in the current system. These frequencies are expected from additional optical confinement (see Chapter 3). The phase rate would be 20-times lower without this additional confinement. Figure 2.3 shows the numerical calculation for the average interaction phase per time $\mu = \frac{\phi_{\downarrow\downarrow}}{t}$ as well as the relative standard deviation of the phase per time. As expected, the phase rate decreases for higher temperatures and the spread of collisional phase due to thermal motion increases rapidly, indicating that ground-state-cooled atoms are needed. From this simulation I deduce that the standard deviation of the phase for the atoms at present radial temperature should be even higher, making interactions between atoms hard to be detected.

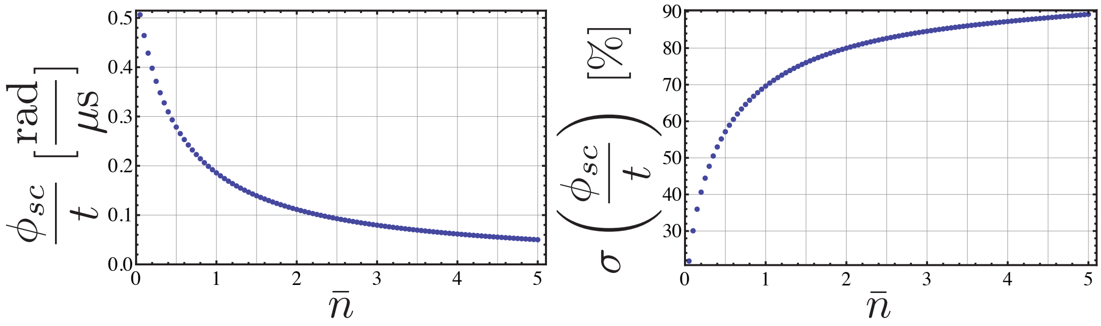

Figure 2.3: Left: Absolute value of the simulated phase rate in $[\frac{\text{rad}}{\mu\text{s}}]$ Right: relative standard deviation of the simulated phase rate in [%].

In experiments the phase $\phi_{\uparrow\downarrow}$ is measured through quantum interference and detection of the spin populations of the atoms. The signal for the sequence suggested above follows $\cos^2$ if the atoms are always in the same state in all directions. For atoms in a thermal state the signal washes out with higher temperature. Scanning the phase ϕ_{MW} of the last $\frac{\pi}{2}$ pulse for a constant interaction time t changes the measured phase and a Ramsey like fringe can be measured. The contrast C of the fringe is defined via:

$$P_{\uparrow}(t) = \frac{1}{2}\left(1 - C\cos\left(\phi_{\uparrow\downarrow}t + \phi_{\mathrm{MW}}\right)\right). \tag{2.12}$$

Measuring the population $P_{\uparrow}$ subsequent at two different phases of the last $\frac{\pi}{2}$ microwave pulse, e.g. $\phi_{\mathrm{MW}} = 0$ ($P_{\uparrow}(0,t)$) and $\phi_{\mathrm{MW}} = -\frac{\pi}{4}$ ($P_{\uparrow}(t, -\frac{\pi}{4})$) is sufficient to determine the phase $\phi_{\uparrow\downarrow}$ and the contrast C. The contrast C and the phase $\phi_{\downarrow\uparrow}$ are extracted from these probabilities as:

$$C = \sqrt{\left(2P_{\uparrow}\left(t,0\right)-1\right)^2 + \left(2P_{\uparrow}\left(t,-\frac{\pi}{4}\right)-1\right)^2} \tag{2.13}$$

$$\phi_{\uparrow\downarrow} = \begin{cases} \arctan\left(\frac{2P_{\uparrow}(t,0)-1}{2P_{\uparrow}\left(t,-\frac{\pi}{4}\right)-1}\right) + \frac{\pi}{2} & \text{for } P_{\uparrow}\left(t,-\frac{\pi}{4}\right) \geq 0.5 \\ \\ \arctan\left(\frac{2P_{\uparrow}(t,0)-1}{2P_{\uparrow}\left(t,-\frac{\pi}{4}\right)-1}\right) + \frac{3\pi}{2} & \text{else.} \end{cases} \tag{2.14}$$

The resulting behavior is shown in Figures 2.4 and 2.5. As expected from the previous calculation the phase rate decreases with increasing mean vibrational states. For higher mean vibrational states the contrast decay is slower because also the absolute phase fluctuation is also smaller. Further studies of the overlap integral (see Appendix A) reveal that the phase rate for two atoms in given vibrational states is determined by a constant multiplied by a rational number which depends on the vibrational quantum numbers. This allows revivals of the contrast because there are interaction times where several different involved states have the same interaction phase modulo 2π . This effect has been seen in interacting Bose-Einstein-Condensates where only discrete interaction energies are possible [25]. The effect is not so dominant in the situation discussed here as the thermal averaging is done over the cosine squared of these discrete interaction phases. One can expect that the phase rate decreases further for mean vibrational quantum numbers higher than simulated. At the same time the contrast is expected to increase again as the absolute phase deviation also decreases. This is based on the assumption in this simulation that no interaction phase would lead to a signal with perfect contrast. Realization of a defined phase to implement algorithms is not possible in this regime as the interaction time to reach a defined phase will increase as $\bar{n}$ increases.

Both simulations clearly indicate that atoms have to be cooled to the motional ground-state in all directions with a very high fidelity. Also, a reasonable phase rate can only be achieved in a deep trap with high axial as well as radial trapping frequencies. In Chapter 3, I will propose a possibility to increase the radial trapping frequencies and attain ground-state cooling of the radial degrees of freedom (Chapter 4). Simulations including the overlap process have been presented by [10]. More in depth calculation on dedicated servers could be done with higher $\bar{n}$ and could also include more experimental details as for example the overlap process.

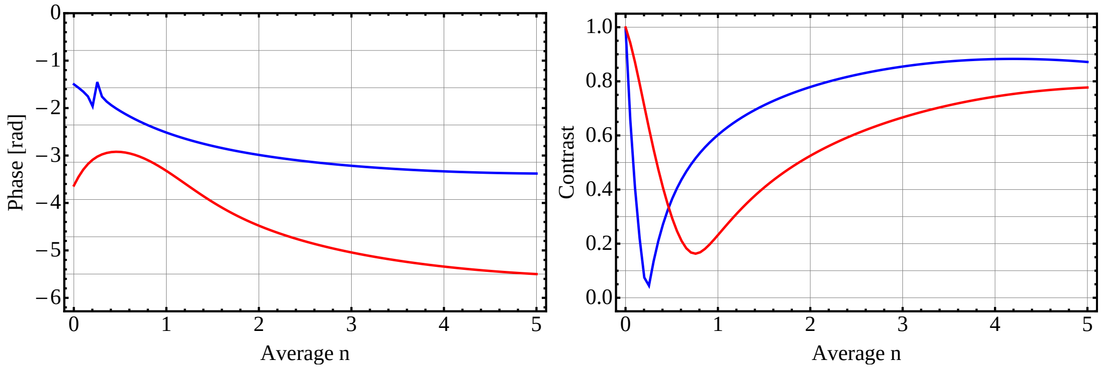

Figure 2.4: Left: Phase vs. $\bar{n}$; Right: Contrast vs. $\bar{n}$. Both quantities are plotted for a interaction time of 5 µseconds (blue) and for 20 µseconds (red). The contrast decreases for increasing $\bar{n}$ before it increases again. This increase can be explained by the smaller phase rate.

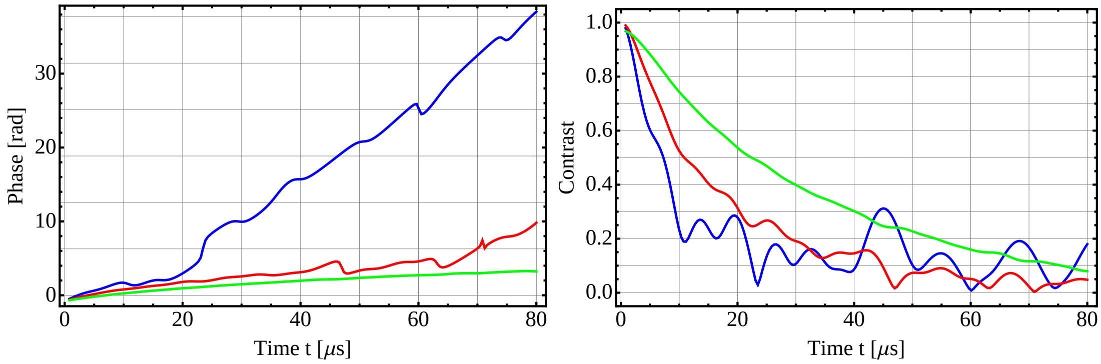

Figure 2.5: Left: Unwrapped phase vs. interaction time t; Right: Contrast vs. interaction time t. Both quantities are plotted for $\bar{n} = 1{,}2{,}4$ (blue, red, green). As expected the phase rate decreases with increasing $\bar{n}$. Jumps in the phase might arise from uncertainties during unwrapping. At lower $\bar{n}$ one can see revivals of the contrast. For higher $\bar{n}$ more states have a significant contribution to the overall phase and the effect averages out.

3 Doughnut shaped optical dipole trap

The trapping frequencies in radial direction have to be increased to use resolved sideband cooling to prepare atoms in the motional ground-state. As described in Section 2, this is needed to investigate cold collisions. Furthermore, initializing atoms in the ground-state will also bring significant advantages in terms of longer coherence time, thus enabling us to perform complex experimental sequences. The plan here is to superimpose a blue detuned beam with a hole at the center on top of the 1D lattice to increase the confinement in radial direction. Such a beam is called a doughnut beam. It is an advantage of this method that the atoms will be trapped at the dark center of the beam. Hence, the trapping frequency can be increased and at the same time the scattering rate can be kept low [17]. This scheme is compatible with present optical access, as the doughnut beam will be superimposed on the 1D lattice in front of the vacuum glass cell where atoms are trapped. The blue detuned doughnut beam represents a cost effective solution to the need of increasing transverse confinement since the wavelength can be chosen close to the atomic D_2 transition of Cs atoms.

In this chapter, I will describe the experimental realization of the doughnut shaped optical dipole trap and address problems which I encountered during the experiments. At the end of the chapter, I will present first measurements done with this setup.

3.1 Present experimental setup

The current apparatus was designed to show state dependent transport in an optical lattice and has recently been used to realize a quantum mechanical analogue of classical random walks [13]. Figure 3.1 gives an overview of the setup, which I will describe shortly. Detailed information can be found in PhD and Master theses and journal articles from our research group.

The experiments are done under ultra high vacuum at a pressure of $3 \cdot 10^{-11}$ mbar inside a glass cell. We use neutral cesiums atoms for the experiment as well established techniques exist to control these atoms. The Cs is provided by a reservoir connected to the vacuum chamber via a valve to control the Cs pressure. The outermost Zeeman sub-levels of the hyperfine ground-state, $|{\uparrow}\rangle = |F = 4, m_F = 4\rangle$ and $|{\downarrow}\rangle = |F = 3, m_F = 3\rangle$, are used as a quasi two-level system. Magnetic fields lift the degeneracy of the Zeeman sub-levels and tunes the transition frequency between $|{\uparrow}\rangle \leftrightarrow |{\downarrow}\rangle$ sufficiently far away from transitions between other Zeeman sub-levels of these two hyperfine levels. Primed (non-primed)

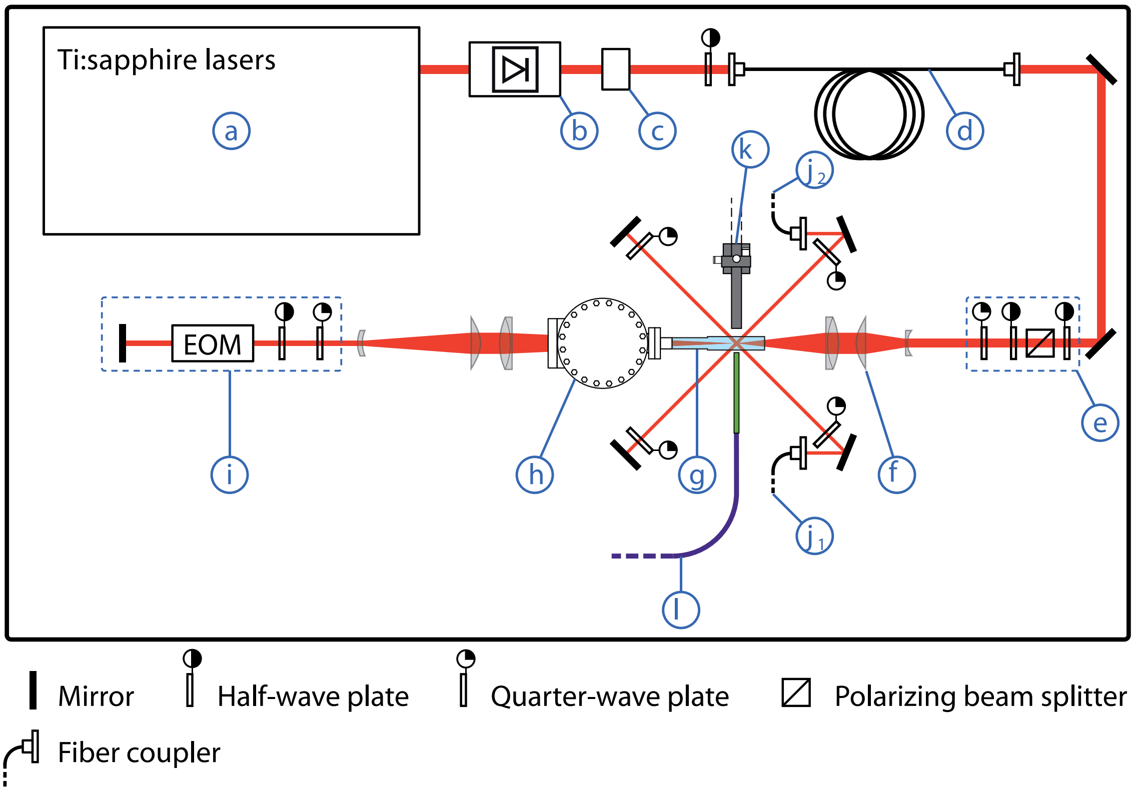

Figure 3.1: Schematic overview of the current optical setup: The Ti:sapphire laser (a) produces the laser beam for the optical lattice which passes through an optical isolator (b) and an AOM (c) used for power control. The beam further passes through a optical fiber (d), a polarization control setup (e), a lens system (f) and is focused in a glass cell (g) which is attached to the vacuum chamber (h). Thereafter it enters the polarization control used for the state dependent transport and is retro-reflected. (j1) and (j2) indicate two of three MOT beams, defining the x and y-axes, respectively. The third beam is perpendicular to the sketched plain. (l) is the microwave antena used for single qubit operations and (k) is first part of the imaging system. According to [24].

quantum numbers refer to the $6^2P_{3/2}$ ($6^2S_{1/2}$) electronic state of Cs.

All experimental sequences start with the magneto optical trap (MOT). The average number of loaded atoms can be adjusted by the field gradient strength. The Doppler limited temperature of the MOT is 125 µK. Sub-Doppler cooling mechanisms lead to lower temperature of the order of 10 µK [24]. After that between one and fifty atoms are loaded into the optical dipole trap. A retro-reflected laser beam from a Ti:sapphire laser forms a standing wave with a periodicity of $\frac{\lambda_{DT}}{2}$ defining the optical dipole trap. The laser has a wavelength of $\lambda_{DT} = 865.9\,\text{nm}$, especially chosen to allow state dependent transport. For this wavelength, the $|\uparrow\rangle$ state couples only to σ^+ polarized light and the $|\downarrow\rangle$ couples with

$\frac{7}{8}$ to σ^- and only with $\frac{1}{8}$ to σ^+.
The electro-optic modulator (EOM) shifts in a controllable manner the phase of the back reflected beam and thus shifts the lattices for the two used cesium states, with respect to each other [24]. The relevant physical parameters of the atoms inside the dipole trap can be found in Table 3.1.

Parameter	Value
Axial trapping frequency	115 kHz
Radial trapping frequency	1 kHz
Scattering Rate	10 Hz

Table 3.1: Relevant parameters characterizing the present dipole trap [24].

The Cs atoms inside the dipole trap are further cooled with the optical molasses formed by the same beams used for the MOT but with disabled magnetic field gradient. After that, the atoms are optically pumped to the initial $|\uparrow\rangle$ state. For that a σ^+-polarized laser beam, resonant with the $F = 4 \rightarrow F' = 4$ transition is applied. A beam of the repumping laser, stabilized to the $F = 3 \rightarrow F' = 4$ transitions, ensures that the atom is transfered back to the optical pumping cycle whenever it decays to the $F = 3$ ground-state [26].
Microwave radiation and the capability to shift the lattice allow us to cool the axial degree down to the ground-state with a probability of 97 % [27]. This is described in more detail in Section 4.1.
One central part of the setup is the imaging system which allows us to resolve the single atoms in the lattice potential. When needed, the exact position of each atom in the lattice can be measured for sparse filling. For all sequences fluorescence images of atoms are taken before and after manipulating the atoms. A state-selective push-out is applied before the second picture. Therefore a laser beam resonant to the $F = 4 \rightarrow F' = 5$ transition removes the atoms in $F = 4$ (including state $|\uparrow\rangle$), but leaves the $|\downarrow\rangle$ state unaffected [28].
For the experimental sequences described in this thesis the relevant information to be extracted is the spin state rather than the exact position. During the central part of the sequence, between both images, the quantum state of the atom is currently manipulated with microwave radiation and sideband transitions are enabled by the spin dependent lattice. This gives complete control of the quantum state of the quasi spin $\frac{1}{2}$-system.

3.2 Higher radial trapping frequency with the doughnut beam

In Chapter 2, I showed that ground-state-cooled atoms are needed to measure cold collisions and to use collisions to entangle atoms which requires higher trapping frequencies in radial direction. I will present a way to increase the confinement in radial direction with a blue detuned hollow laser beam. Stronger confinement will also favor resolving motional sidebands in the Raman sideband cooling presented in Chapter 4.

There exist several different approaches to generate a hollow laser beam. Laguerre-Gaussian modes can be converted to Hermite-Gaussian modes which have a dark center. Experimentally the mode-conversion was realized by [29]. Hollow beams can also be obtained by computer generated holograms which are illuminated by a Gaussian beam [30]. For my experiment a spiral phase plate (SPP) will be used to generate the doughnut beam. The thickness of the SPP increases proportional to the azimuthal angle as shown in Figure 3.2. This imprints a phase factor to the wavefront which is a function of the azimuthal angle: $e^{il\phi}$, where l is called the topological charge. It is given by

$$l = \frac{\mathit{\Delta} n \cdot h}{\lambda} \tag{3.1}$$

Here $\mathit{\Delta} n$ denotes the difference of the refractive index of the material of the SPP to its surrounding, λ is the wavelength of the incident laser beam and h is the maximal height of the SPP structure as shown in Figure 3.2. I use a SPP manufactured by RPC photonics.

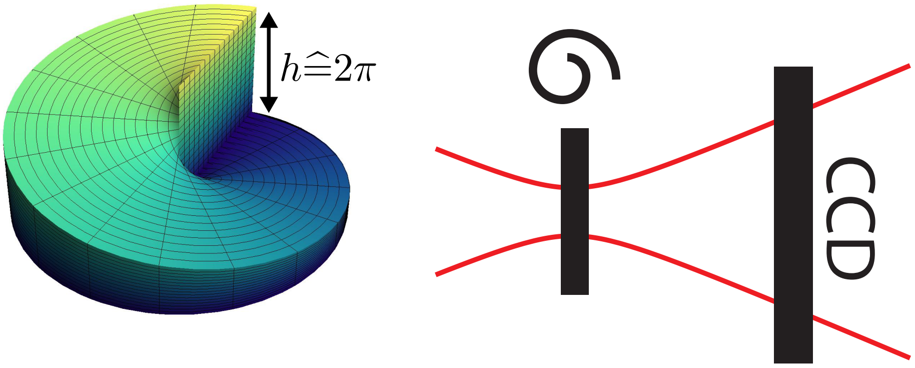

Figure 3.2: Left: Illustration of a spiral phase plate imprinting a phase pattern depending on the azimuthal angle on the incident beam. The height h of the step corresponds to a phase difference of 2π. Two opposite points have a phase difference of π and interfere destructively in the far field. Right: The SPP in this setup is placed at the focus of a Gaussian beam. Figure 3.3 illustrates the intensity profile of the Gaussian beam at the position of the CCD camera and the corresponding doughnut beam.

The electric field of the beam behind the SPP has the distribution:

$$E\left(\rho,\phi,z\right) = E_0 \frac{w_0}{w\left(z\right)} e^{\frac{-\rho^2}{w^2(z)}} e^{-ikz-ik\frac{\rho^2}{2R(z)}+i\zeta(z)} e^{i\phi} \tag{3.2}$$

where

$$\begin{aligned}
k &= \frac{2\pi}{\lambda} && \text{, wave number}\\
w\left(z\right) &= w_0\sqrt{1+\left(\frac{z}{z_R}\right)^2} && ,\frac{1}{e^2}\text{ - beam radius}\\
R\left(z\right) &= z\left(1+\left(\frac{z_R}{z}\right)^2\right) && \text{, curvature radius of the wavefront}\\
\zeta\left(z\right) &= \tan^{-1}\left(\frac{z}{z_R}\right) && \text{, Gouy phase}\\
z_R &= \frac{\pi w_0^2}{\lambda} && \text{, Rayleigh range}\\
E_0 &= \sqrt{\frac{2P}{\pi w_0^2}} && \text{, electric field at } \rho=0,\ \phi=0,\ z=0\\
P & && \text{, power.}
\end{aligned} \tag{3.3}$$

In paraxial approximation the propagation of the doughnut beam through a system of optics can be calculated using the ABCD formalism in the Collins integral. The calculation yields the following result [31]:

$$\begin{aligned}
E_D\left(\rho,\phi,z\right) =& \frac{2\pi}{\lambda B}E_0\frac{w_0}{w\left(z'\right)}\frac{\sqrt{\pi}b}{8a^{\frac{3}{2}}}e^{-ikz}e^{i\frac{kD\rho^2}{2z}}e^{-ikz'+i\zeta(z')}\\
&\times e^{i\phi}e^{-\frac{b^2}{8a}}\left[I_0\left(\frac{b^2}{8a}\right)-I_1\left(\frac{b^2}{8a}\right)\right]
\end{aligned} \tag{3.4}$$

where I_m is the modified Bessel function of the first kind an m-th order and

$$a = \frac{1}{w^2\left(z'\right)}+\frac{ik}{2R\left(z'\right)-\frac{iAk}{2B}} \tag{3.5}$$

$$b = \frac{k\rho}{B}. \tag{3.6}$$

The doughnut beam is still very similar to the incident Gaussian beam in the tails but presents a dip down to zero intensity at the center. The doughnut beam and the Gaussian beam are compared in Figure 3.3.

The doughnut beam is blue detuned with respect to the D_2 line and even further with respect to the D_1 line of Cs; atoms are pushed towards positions with low intensity. The

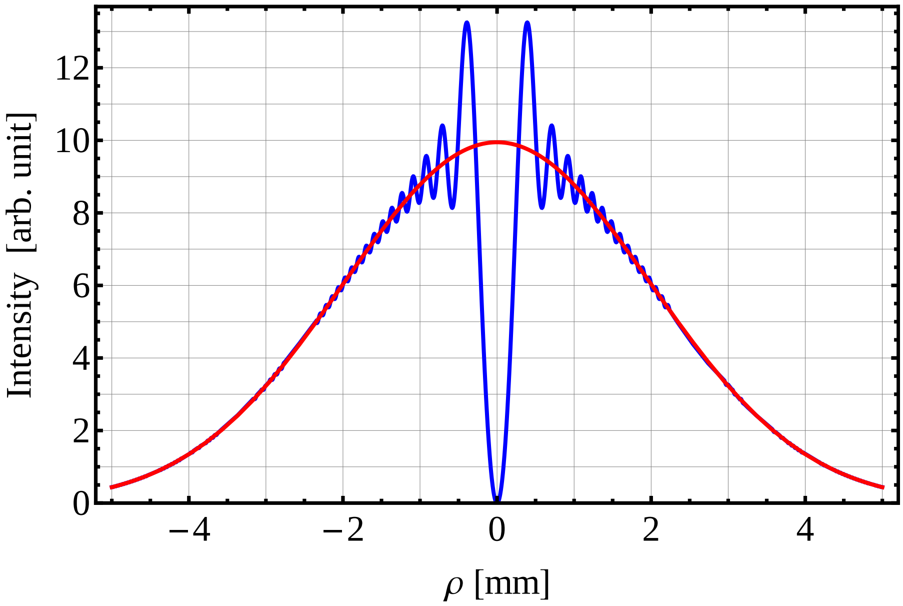

Figure 3.3: Beam profile of a Gaussian beam (red) and the corresponding doughnut beam (blue). The Gaussian beam has a beam waist of $w_0 = 4\,\mathrm{mm}$ and the SPP is placed at the focus. The beam profile is shown for a position of 100 mm after the SPP. The setup with the SPP is shown in Figure 3.2.

dipole potential for this situation with big detuning $\varDelta$ simplifies to [17]:

$$U_{dip}\left(\rho,\phi,z\right) = \frac{3\pi c^2}{2\omega_{\mathrm{D}_2}^3}\frac{\varGamma}{\varDelta} I\left(\rho,\phi,z\right), \tag{3.7}$$

where only the D_2 line with the resonance frequency ω_{D_2} and linewidth $\varGamma$ is considered, while the D_1 is neglected because it is far off resonant. The intensity distribution

$$I_D\left(\rho,\phi,z\right) = \frac{c\varepsilon_0}{2}\left|E_D\left(\rho,\phi,z\right)\right|^2 \tag{3.8}$$

of the doughnut beam can be approximated to second order in ρ around the position $\rho = 0$ [31]. The dipole potential in this harmonic approximation reads:

$$U_{dip}\left(\rho,\phi,z\right) = \frac{3\pi c^2}{2\omega_{D2}^3}\frac{\varGamma}{\varDelta}E_0^2\frac{\pi k^4 w_0^6}{64B^4 w^2\left(z'\right)\left|a\right|^3}\rho^2 + O\left(\rho^4\right). \tag{3.9}$$

This results in a trap frequency of:

$$\omega_\perp = \sqrt{\frac{3\pi P\varGamma}{m\varDelta\left|a\right|^3}\frac{ck^2w_0^2}{16B^2 w\left(z'\right)}}. \tag{3.10}$$

This denotes that the radial trap frequency scales with the power as $\omega_\perp \propto \sqrt{P}$ and with the beam waist radius of the Gaussian beam as $\omega_\perp \propto w_0^2$. The behavior of this formula depending on the different parameters is discussed in more detail in [31].

3.2.1 Laser system

An optical trap operating close to a resonance is deeper and has higher trapping frequencies but at the same time the scattering rate increases faster when approaching a resonance. To avoid the need of a high power laser system, the doughnut laser beam is tuned relatively close to the D_2 line of the Cs atoms on the blue side of the transition. For my purpose I set up an external cavity diode laser (ECDL) in combination with a tapered amplifier (TA). This system is referred to as master oscillator power amplifier (MOPA). The output power of the TA depends on the current running through the TA and also on the power seeded into the TA. The measurements of these dependencies are displayed in Figure 3.4. The output power does not show a saturation effect and it seems that higher output power could be reached by either increasing the amount of seeded power or the current through the TA. The manufacturer specifies the maximum output power with 1.2 W. At higher light intensity the output surface of the TA could be damaged.

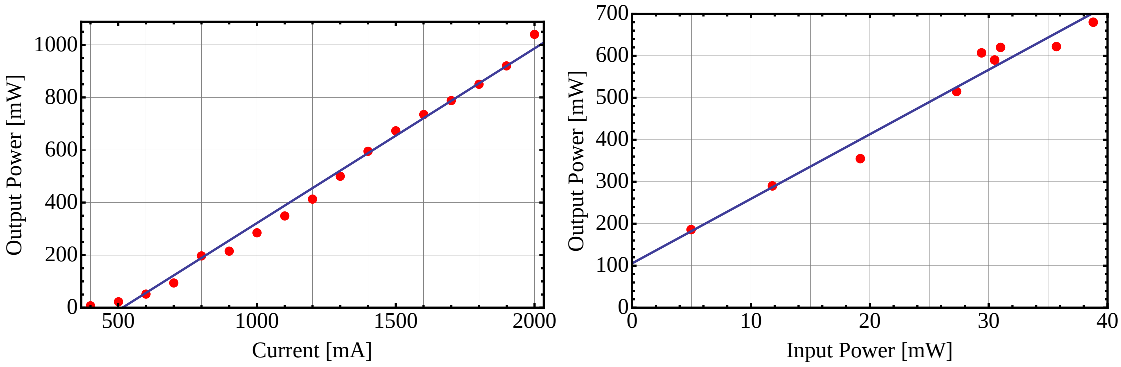

Figure 3.4: Left: Output power of the TA versus current with linear fit at 39 mW input power; Right: Output power of the TA versus input laser power at a current of1500 mA, both indicate that with a higher current or higher input laser power more output power could be reached.

3.2.2 Spacial and spectral filtering

The laser mode leaving the TA has a strong astigmatism as it diverges differently in the two axis. This is compensated using a collimation system composed of three lenses: a aspherical lens, a convex lens and a cylindrical lens. The aspherical lens has a focal length of 3.2 mm and numerical aperture of 0.55. This lens is placed directly after the TA chip to cancel the strongest divergence and to collect most of the light. The normal convex lens and the cylindrical lens are used to collimate both axes and to match the size of the beam in both axes. This is illustrated in Figure 3.5. The final spacial mode cleaning is done by fiber coupling the light. At the fiber approximately 50% of the light is lost. This is due to not perfect fiber coupling and due to non Gaussian mode of the TA. The mode leaving the fiber can be assumed to have perfect Gaussian shape.

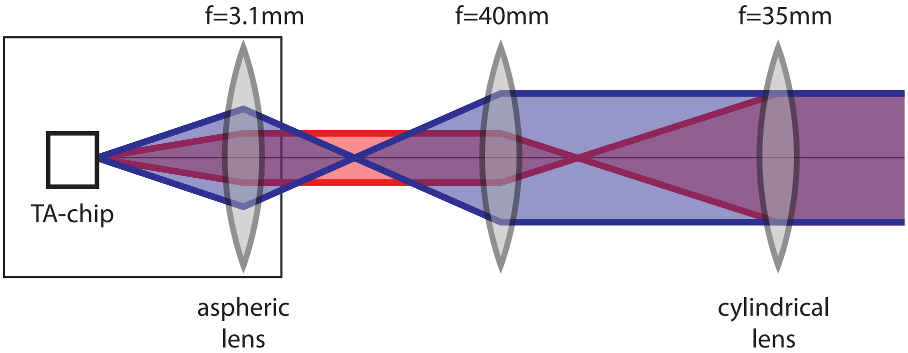

Figure 3.5: Tapered amplifier collimation, not to scale: Red indicates the fast axis and blue the slow axis. The lenses are chosen such that beam size is equal for both axes and is optimized for the fiber coupler.

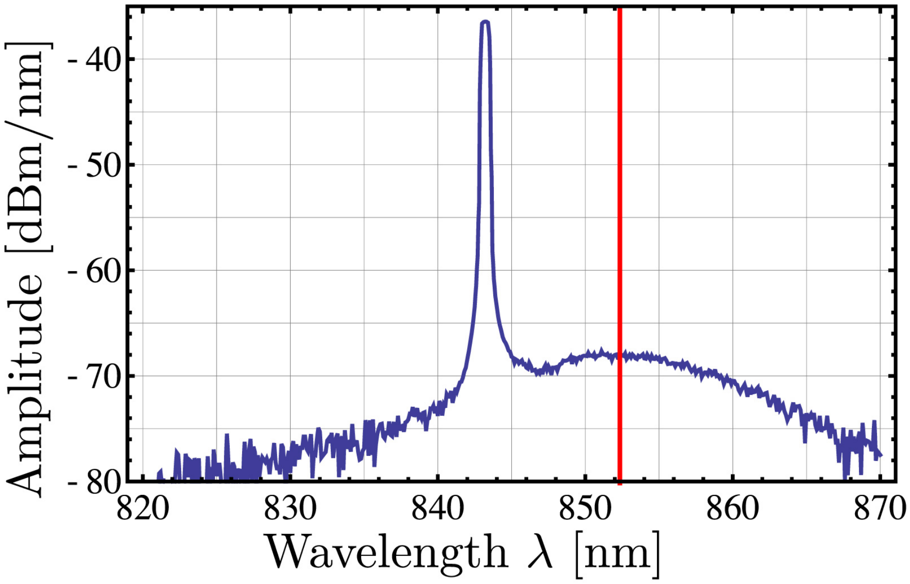

Figure 3.6: Spectrum of the tapered amplifier: The vertical red line indicated the position of the cesium D2-line.

Figure 3.6 shows the spectrum of the light after the TA. You can see the amplified light and a broad pedestal. This pedestal is due to spontaneous emission inside the TA. The TA does not have a resonator which would efficiently reduce the spontaneous emitted light.

The broad pedestal could induce transitions at resonant frequencies of Cs atoms. This would heat the atoms and should be filtered out. For this reason a heated Cs cell will be placed between the TA and the optical fiber. From the measurement in Figure 3.6 the pedestal is about 10^5-times weaker than the amplified light. The integrated relative amount of light resonant with the cesium D2-line using the natural linewidth is: $3 \cdot 10^{-7} \cdot P_{\text{total}}$. It is important to know the scattering rate of this light compared to the scattering rate of the resonant rate to decide if filtering is necessary.

For this, atoms are modeled as a classical ensemble in thermal equilibrium at a temperature of $T = 10\,\mu\text{K}$. Only the two radial directions have to be considered. The motion in axial direction leads to Doppler broadening of the absorption line. The two radial axes are decoupled and the atoms have the same temperature in each direction. The probability $P(E)$ to find a atom with energy E follows the Boltzmann distribution:

$$P_B(E) = \frac{1}{k_B T} e^{-\frac{E}{k_B T}}. \tag{3.11}$$

The classical probability density function for a atom with energy E in a potential $U(x) = m\Omega^2 x^2/2$ is:

$$P_E(x) = \begin{cases} \frac{1}{\pi\sqrt{\frac{2E}{m\Omega^2} - x^2}} & \text{for } |x| \geq \sqrt{\frac{2E}{m\Omega^2}} \\ \\ 0 & \text{else.} \end{cases} \tag{3.12}$$

The spatial density function for a thermal average is the integral of $P_E(x)$ over all energies E weighted with the corresponding probability [32]:

$$P_{th}(x) = \int_0^\infty P_E(x) P_B(E)\, dE \tag{3.13}$$

$$= \sqrt{\frac{m\Omega^2}{2\pi k_B T}} e^{-m\Omega^2 x^2/(2k_B T)} \tag{3.14}$$

This density distribution is assumed along both radial direction. The intensity I to which a atom inside the doughnut beam is exposed to is given by the overlap of the radial intensity distribution of the doughnut beam $I_D(r)$ and the density distribution:

$$I = 2\pi \int_0^\infty r I_D(r) \frac{m\Omega^2}{2\pi k_B T} e^{-m\Omega^2 r^2/(2k_B T)} dr \tag{3.15}$$

Knowing the average light intensity the scattering rate can be calculated for the resonant light with [33]:

$$R_{SC} = \left(\frac{\mathit{\Gamma}}{2}\right) \frac{I/I_{sat}}{1 + I/I_{sat}} \tag{3.16}$$

where $\mathit{\Gamma}$ is the natural linewidth and I_{sat} is the saturation intensity. For the peak with larger detuning $\mathit{\Delta}$ the following approximation is valid [17]:

$$R_{SC} = \frac{3\pi c^2}{2\hbar\omega_{D_2}^3} \frac{\mathit{\Gamma}}{\mathit{\Delta}} I. \tag{3.17}$$

Using the doughnut beam parameters described in Section 3.3 results in a scattering rate of 345 Hz for the peak and 23 kHz for the resonant light. This indicates that spectral filtering of the resonant light is needed.

3.2.3 Integration into the current setup

The doughnut beam has to be overlapped with the existing dipole trap. This could be done with polarizing or non-polarizing beamsplitter cubes but either solution limits the polarization or bisects the available power, respectively. I rather decided to combine the two laser beams with a dichroic mirror reflecting the doughnut beam while transmitting the dipole trap beam. The specification of the mirror can be found in Table 3.2.

This configuration reduces losses and keeps the free choice of polarization compared to the options with a beamspitter. The doughnut beam can be overlapped with the dipole trap on either side of the glass cell as the telescopes on both sides of the glass cell are comparable. Placing the dichroic mirror on the same side as the fiber coupler (on the right side of the glass cell in Figure 3.7) of the dipole trap has the advantage that all polarization disturbances of the dichroic mirror can be filtered and precompensated by the existing polarizer and waveplates. However this configuration has the drawback that the light will be back reflected just as the beam for the dipole trap. The atoms will be pushed to the nodes of the formed blue detuned standing wave. This effect could be suppressed if the two laser beams are only overlapped at the atoms and misaligned for longer distances. The dichroic mirror could also be placed on the left side of the glass cell. With this configuration one eliminates the standing wave for the doughnut beam. However it affects the polarization of the dipole trap. Right now the relative polarization extinction of the back reflected dipole beam is in the order of 10^{-4} and can be rotated in a controllable

wavelength λ	measurement	s-polarization	p-polarization
850 nm	Reflectivity	>97 %	>65 %
866 nm	Transmittance	>60 %	>80 %

Table 3.2: Specification of the dichroic mirror provided by the LASER COMPONENTS GmbH

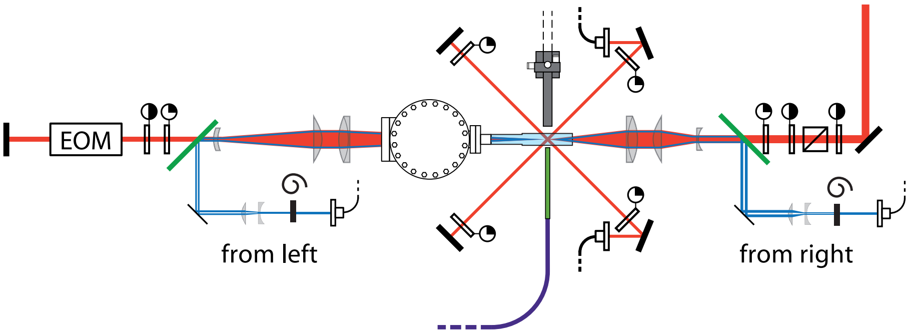

Figure 3.7: The doughnut beam can be integrated from both sides of the glass cell with a dichroic mirror (geen): From the right side the doughnut beam forms a standing wave and from the left side the polarization of the retro-reflected beam is affected as discussed in Section 3.2.3.

manner to any desired linear polarization. This is needed for the state dependent lattice. The birefringent dichroic mirror can be compensated for only one given polarization of the dipole trap beam. If a voltage is applied to the EOM to rotate the polarization of the back reflection of the dipole trap beam, the dichroic mirror is not compensated anymore and the relative extinction ratio increases to 10^{-1}. The amount of power back reflected to the atoms would also depend on the polarization with this configuration as the transmittance of the dichroic mirror is polarization dependent. This would prevent the current experiments because they rely on a good state dependent transport which is very sensitive to polarization inhomogeneities.

The dichroic mirror could also be placed on the left side of the glass cell. With this configuration one eliminates the standing wave for the doughnut beam. However it affects the polarization of the dipole trap. Right now the relative polarization extinction of the back reflected dipole beam is in the order of 10^{-4} and can be rotated in a controllable manner to any desired linear polarization. This is needed for the state dependent lattice. The birefringent dichroic mirror can be compensated for only one given polarization of the dipole trap beam. If a voltage is applied to the EOM to rotate the polarization of the back reflection of the dipole trap beam, the dichroic mirror is not compensated anymore and the relative extinction ratio increases to 10^{-1}. The amount of power back reflected to the atoms would also depend on the polarization with this configuration as the transmittance of the dichroic mirror is polarization dependent. This would prevent the current experiments because they rely on a good state dependent transport which is very sensitive to polarization inhomogeneities.

The advantages of these two positions of the dichroic mirror can be combined if a so called two arm setup is used. The dipole trap of the current setup is formed by a single retro-reflected beam. This configuration is also called single arm setup. For the two arm setup the dipole trap laser beam is split and sent to the atoms from two independent directions. The two counter propagating beams are overlapped and form again a standing wave. With this configuration the doughnut beam cannot form a standing wave and the polarization is also not affected with the dichroic mirror on the right side. This setup needs twice as much power in the laser beam of the dipole trap to reach the same trapping frequency which is not a limiting requirement with the present setup. The EOM has a limiting retardation capability and must be operated in double pass. This can be overcome with a new EOM. A recently bought EOM has a sufficiently higher retardation capability and the polarization purity seems to be in the same order of magnitude. Measurements with this new EOM, with longer crystals, inside the current setup have proven that the new EOM can work as well as the former one. A schematic illustration illustrates this setup in Figure 3.8.

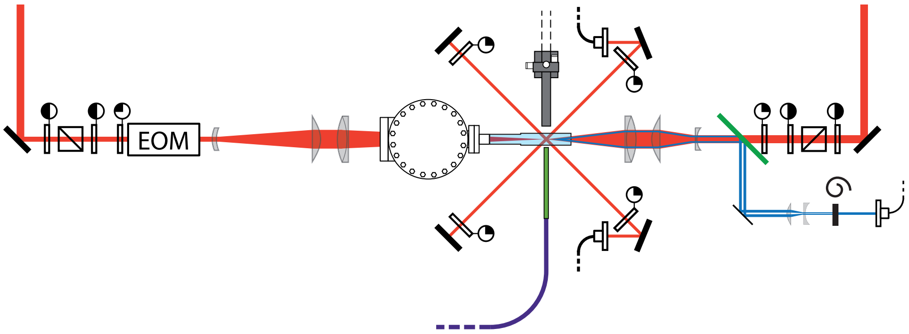

Figure 3.8: Two arm optical lattice: Instead of using a retro-reflected beam the lattice is formed by two counterpropagating lasers. This avoids the problem of a standing wave of the doughnut beam.

3.3 Trap parameters

The telescopes before and after the glass cell have been optimized for the optical lattice and I intend to use them for the doughnut beam as well. The doughnut beam should also be collimated at the position of the telescope because the focus of the doughnut beam should be at the same position as the focus of the dipole trap beam. The doughnut beam has two free parameters which can be used to tune the trapping frequencies: intensity and diameter at the focusing telescope. Equation 3.4 describes the propagation of the doughnut beam for any optical system described by ABCD matrices. This is used to calculate the expected shape of the beam to check for any possible clipping as well as to calculate the resulting trap parameters. The calculations presented here are done for the telescope on the right side of the glass cell (see Figure 3.7). The calculation for the other direction would provide similar results. The light intensity used in my calculation is 250 mW. This was the maximum which could be reached with the available laser source. The highest trapping frequency can be attained for the largest initial beam waist. This results in the shortest Rayleigh length. A initial beam waist of 4 mm is a good compromise.

It corresponds to a Raleigh length of 345 µm, 3 times the maximum loading range of the atoms, and furthermore the existing lenses do not have to be changed. The trapping frequency in this configuration is 21 kHz. The scattering rate as calculated in Section 3.2.2 is 345 Hz. Higher scattering rates can not be tolerated because it would limit the time of each experimental sequence. Higher trapping frequencies and at the same time lower or equal scattering rates can be accomplished with a larger detuning. This requires a new SPP and in addition a new laser source. The SPP produces a perfect doughnut beam only for a single wave length and the current laser source is limited to a small range close to the D_2 line of Cs.

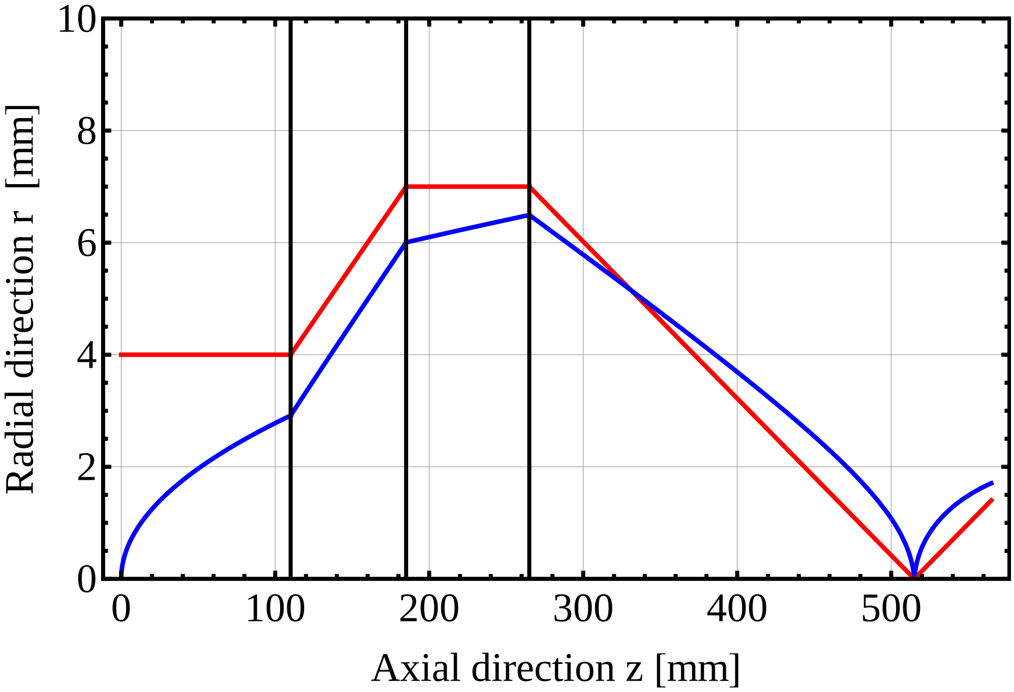

Figure 3.9: The propagation of the doughnut beam is calculated using ABCD matrices. The red line indicates the radial distance of intensity maximum and the blue line indicates the beam waist of the corresponding Gaussian beam without the SPP. The solid vertical black line indicate the positions of the lenses. The beam is not clipped at any lens as the first lens is 25 mm and the others are 50 mm in diameter. For this configuration radial trapping frequencies of 21 kHz are calculated.

3.4 First results

I will conclude this chapter by presenting first results of atoms confined in the blue detuned doughnut beam. For first measurements the dichroic mirror is placed on the right side as described in Section 3.2.3 but without the SPP inside the beam path. A clearly visible beat note between the two standing waves of the dipole trap laser and the doughnut beam laser can be produced. Overlap between both lasers can be guaranteed with a pinhole right after the dichroic mirror and a second pinhole right before the mirror for the back reflection. Lattice sites are empty which would be occupied without the extra blue detuned laser, because the blue detuned laser light pushes the atoms to lower intensities while the red detuned light pulls the atoms to higher intensities. The dipole trap laser has a wavelength of 866 nm and the doughnut beam laser a wavelength of 849.9 nm. This results in a periodicity of $\frac{2\pi}{46\,\mu\mathrm{m}}$ for this beat structure. The measurement, shown in Figure 3.10, agrees with this calculation.

The SPP was inserted into the setup, even so the interference effect was visible, which inhibits a homogeneous increase of the radial trapping frequency. However no effect on atoms trapped inside the optical lattice was visible. It was not possible to find a configuration which suppressed the back reflection and which at the same time ensured that the focuses of the doughnut beam and dipole trap were overlapped.

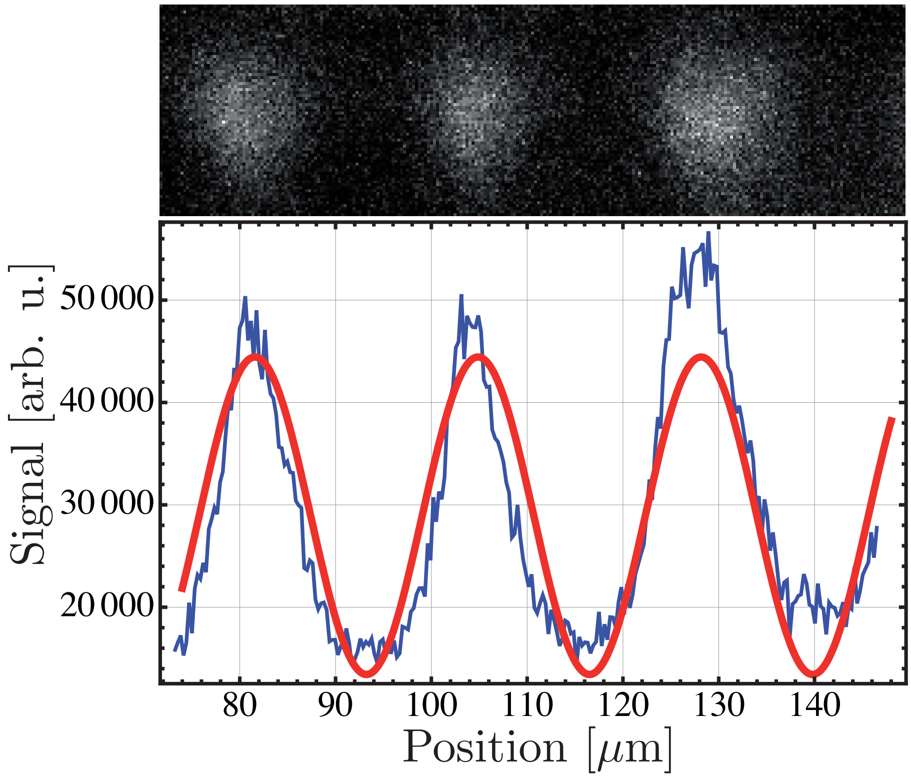

Figure 3.10: Beat note between both dipole trap lasers: The upper picture shows the fluorescence picture of the atoms inside the dipole trap. The lower graph shows the histogram of the intensity and a fit to this data. The periodicity of the pattern is $\frac{2\pi}{47\,\mu\mathrm{m}}$ which agrees to the expected value of $\frac{2\pi}{46\,\mu\mathrm{m}}$.

Although the other configuration with the dichroic mirror on the left side does not allow state dependent transport it was used to demonstrate the increased confinement due to the doughnut beam avoiding a standing wave. The overlap between the doughnut beam and the optical lattice is optimized by coupling the doughnut beam to the fiber of the dipole trap. The coupling efficiency is low because the beam profile is non Gaussian.
I trapped very few atoms inside the dipole trap once with and once without the doughnut beam such that a single atom could be isolated. Several pictures with a single atom at the same lattice position were taken and fitted with a Gaussian distribution in the radial and the axial direction as well. These images were overlapped with each other after shifting the maximum to the same position. This increased statistics and resolution. The final data is shown in Figure 3.11. The extension of the atoms in the radial direction was decreased by approximately 30 % while the extension in axial direction was not affected significantly. The resolution along this axis is limited by the resolution of the imaging system. If only the trapping frequency would have changed the decreased size in radial direction corresponds to an increase in trapping frequency of almost 2. However there are many parameters that can have changed which make it difficult to predict the actual trapping frequency. It was not expected to reach trapping frequencies in the order of 20 kHz as the beam size was not increased with a telescope, reducing the highest possible trapping frequency by a factor of 4. Further the collimation was optimized such that the coupling efficiency to the fiber for the standing wave is highest without the SPP. The advantage of this configuration is that the overlap can be measured quantitative without any extra components, but is not the alignment with highest trapping frequency.

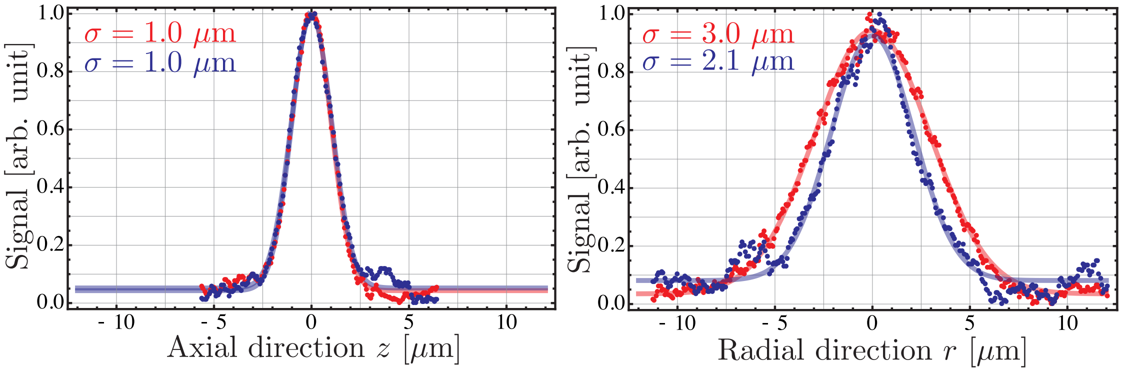

Figure 3.11: Fluorescence Light distribution of the trapped atoms recorded on the CCD camera are fitted with a normal distribution and the corresponding variances σ are written down. Left: The variances in axial direction is limited by the resolution of the imaging system, no change was expected here. Right: The variance in radial direction is reduced by more than 20 % with the doughnut beam turned on. This can be attributed to increased trapping frequencies in radial direction.

4 Resolved Raman sideband cooling

As this experiment works with single atoms, measurements have to be repeated several times to retrieve the quantum mechanical information in the system. Several observable quantities depend on the motional state of the atoms; thermal motion results in a degradation of the signal or even in the complete impossibility to measure the physical effect, as in the case of cold collisions. In this chapter I will address this problem by cooling the atoms to the motional ground-state in radial direction.

4.1 Sideband transitions in an optical lattice

The Cs atoms are trapped inside a deep optical trap as described in Section 3.1, inducing quantized vibrational levels. Transitions between two states of the atom which also change the vibrational states are called sideband transitions. These transitions are illustrated for the two relevant states of cesium in Figure 4.1. Transitions which lower the vibrational quantum number belong to the red sidebands and those which increase the vibrational quantum number to the blue sidebands, when the transitions start at the energetic higher state.

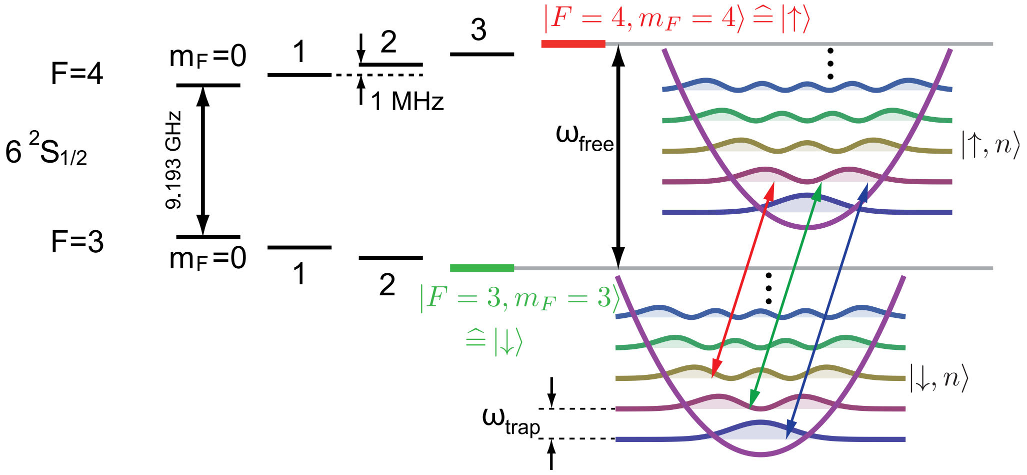
F=4
$6\,^2S_{1/2}$
F=3
$m_F=0$
9.193 GHz
$m_F=0$
1
2
3
1 MHz
1
2
$|F=4, m_F=4\rangle \mathrel{\widehat{=}} |\uparrow\rangle$
ω_{free}
$|\uparrow, n\rangle$
$|F=3, m_F=3\rangle$
$\mathrel{\widehat{=}} |\downarrow\rangle$
$|\downarrow, n\rangle$
ω_{trap}

Figure 4.1: Energy level scheme for the two states used as a qubit considering the hyperfine states (internal) and the motional states (external). With a narrow driving field selected sideband transitions with $\Delta n = +1$(red), 0 (green), -1 (blue) or higher can be addressed, starting from the upper level.

The energy of the photon driving the transition between the atom in the initial state $|n,\alpha\rangle$ and the final state $|n',\alpha'\rangle$ has to be equal to the energy difference between the two states. Here n and n' are the vibrational quantum numbers and α and α' represent all the other quantum numbers. In addition to the energy constraint the probability of the transitions depends on the transferred momentum Δk by the photon along the quantization axis of the harmonic oscillator. The transition probability reduced to the vibrational state is given by:

$$\langle n| e^{-i\Delta kx} |n'\rangle = F, \tag{4.1}$$

which defines the Franck-Condon factor F. One can see directly that sideband transitions are forbidden if $\Delta k = 0$ as different vibrational states of a harmonic oscillator are orthogonal to each other. The Franck-Condon factor can be further calculated if the trap is approximated to be harmonic. The calculation of F can be simplified by introducing "ladder operators" used by Paul Dirac:

$$\begin{aligned} \langle n| e^{-i\Delta kx} |m\rangle &= \langle n| e^{-i\Delta k\sqrt{\frac{\hbar}{2m_{Cs}\omega}}\left(a+a^{\dagger}\right)} |n'\rangle & (4.2)\\ &= \langle n| e^{-i\eta\left(a+a^{\dagger}\right)} |n'\rangle . & (4.3) \end{aligned}$$

Here the Lamb-Dicke parameter η with

$$\eta = \Delta k\sqrt{\frac{\hbar}{2m_{Cs}\omega}} \tag{4.4}$$

is introduced. Following the calculations of [34] leads to the analytic result of the Franck-Condon factor $F\left(\eta,n,n'\right)$:

$$F\left(n,n',\eta\right) = e^{-\frac{1}{2}(\Delta k)^2}\sqrt{\frac{n_<!}{(n_>)!}}\,(i\eta)^{\Delta n}\,L_{n_<}^{\Delta n}\left(\eta^2\right), \tag{4.5}$$

where $L_n^{\alpha}(x)$ are the generalized Laguerre polynomials. $n_<$ is the minimum of the initial and final vibrational state and $n_>$ the maximum and $\Delta n = |n-n'|$. The ratio between coupling to a higher band and coupling to a lower band for $\eta \ll 1$ is given by:

$$\frac{F\left(n,n+1,\eta\right)}{F\left(n,n-1,\eta\right)} = \sqrt{\frac{n+1}{n}}. \tag{4.6}$$

It implies that the transition probability of increasing the vibrational state is higher than lowering the vibrational state. It is important to resolve individual sidebands because if the sidebands are not resolved this will in average lead to heating.

4.1.1 Microwave-induced sidebands

The two hyperfine ground-states are used in the experiment because of their long lifetime. The transition frequency between those is around 9.192 GHz where microwave generators with very narrow linewidth are commercially available. However, the momentum of a microwave photon compared to optical photons is five orders of magnitude lower. The transfered momentum Δk is too small to drive sideband transitions directly. This problem can be circumvented by shifting the position of the lattice site for the different state and thus the wave functions with respect to each other. The shift of the wave function $|\psi(x)\rangle$ of one state by Δx can be described by the shift operator $T_{\Delta x}$:

$$T_{\Delta x} |\psi(x)\rangle = e^{\frac{-i\Delta xp}{\hbar}} |\psi(x - \Delta x)\rangle . \tag{4.7}$$

This is similar to transferring momentum and will again permit coupling different side band transitions. These sideband transitions in axial direction can be driven with high fidelity [27].

The atoms can be cooled in the axial direction to the motional ground-state with these microwave induced sideband transitions. For this purpose the atoms are prepared in $|\uparrow, n\rangle$ with n representing the quantum number of the vibrational level in the axial direction. The microwave field is tuned to the first blue sideband of the transition $|\uparrow, n\rangle \leftrightarrow |\downarrow, n-1\rangle$, lowering the vibrational level by one as the initial state is energetic higher. A σ^+ polarized repumper laser coupling $|F=3\rangle \leftrightarrow |F'=4\rangle$ pumps the atom to the state $|F'=4, m=4, n-1\rangle$. This state can decay to the state $|\uparrow, n-1\rangle$ by spontaneous emission and the cycle starts again. It is important that the Lamb-Dicke parameter for the repumper laser light η_{rp} is small and thus the absorption and spontaneous emission is unlikely to change the vibrational quantum number. A third laser is used on the transition $|F=4\rangle \leftrightarrow |F'=4\rangle$. This brings the atom which decay spontaneously to $|F=4, m=3\rangle$ back to the cooling cycle. During one cycle the energy $\Delta E_- = \hbar\omega$ is removed and due to the photon recoil of the repumper and spontaneous emission at maximum the energy $\Delta E_+ = 2\frac{\hbar^2 k_{D_2}^2}{2m_{Cs}}$ is added. For cooling this energy balance for a complete cycle has to be negative. This can be written as:

$$\begin{aligned}
1 >& \frac{\Delta E_+}{\Delta E_-} \\
1 >& 2\frac{\hbar^2 k_{D_2}^2}{2m_{Cs}\omega\hbar} \\
1 >& 2\eta_{rp}^2
\end{aligned}$$

This also results in the requirement that the Lamb-Dicke parameter for the resonant light η_{rp} has to be smaller than 1. The cycle is shown in Figure 4.2.

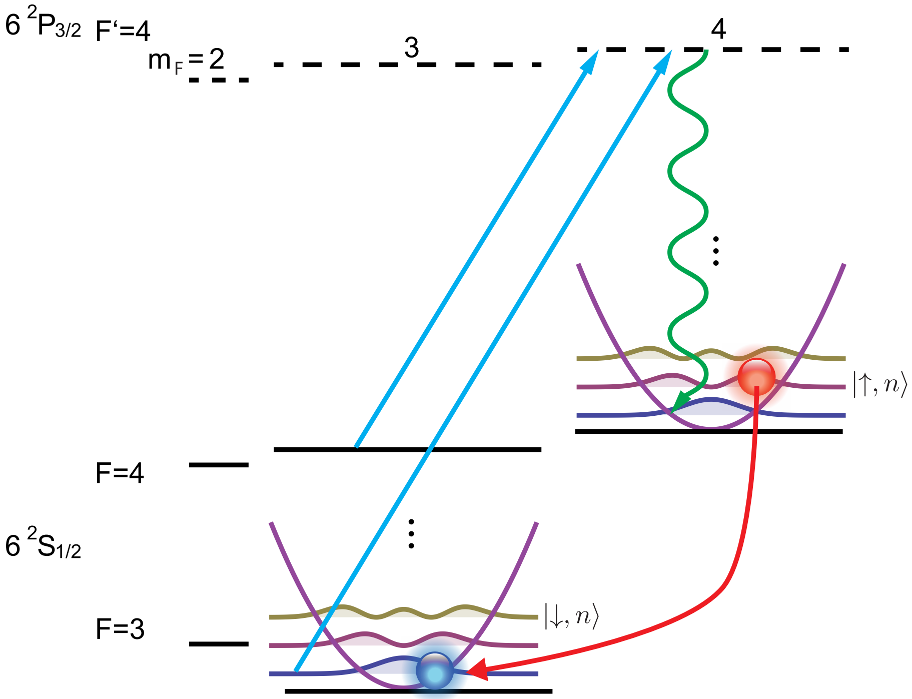

Figure 4.2: Microwave sideband cooling scheme: The cooling cycle starts in the $|\uparrow\rangle$ state. The microwave (red) transfers atoms from $|\uparrow, n\rangle$ to $|\downarrow, n-1\rangle$ which is possible as the lattices for the two different states are shifted with respect to each other. The blue sideband is used to reduce the vibrational quantum number by 1 as the cooling start from the energetic higher state. The repumper laser (blue) pumps the atom up to the $|F'=4, n-1\rangle$ state. From there it can decay spontaneous back to $|\uparrow, n-1\rangle$ (green). The second repumper laser (blue) pumps the atoms back to the cooling cycle which decay to the $|F=4, m=3\rangle$-state.

4.1.2 Two photon induced sidebands

Stimulated Raman transitions use two photons as described in Section 4.2. The atoms get the recoil of an absorbed laser photon of k_R and of the emitted laser photon of k_S. After each scattering event the expectation value for the atomic momentum has changed by $\hbar\Delta k$, where $\Delta k = k_R - k_S$ is the difference between the wave vectors of the absorbed and emitted photon. The momentum of the two photons is nearly the same $|k_R| = |k_S|$ and hence the maximum transferred momentum can be approximated by $2\,|k_R| = 2\,|k_S|$ in the case of opposing beams. For the cooling scheme which I propose in Section 4.3, the two Raman lasers are perpendicular to each other. The resulting momentum vector has an angle of 45° to the radial plane, in which I want to cool the atoms. This leads to an effective Δk^{-1} of $\frac{852\,\mathrm{nm}}{2\pi}$ and a Lamb-Dicke parameter $\eta_{RL} = 0.32$. Figure 4.3 shows the Franck-Condon factor vesus the Lamb-Dicke parameter for different initial states and fixed $\Delta n = 1$.

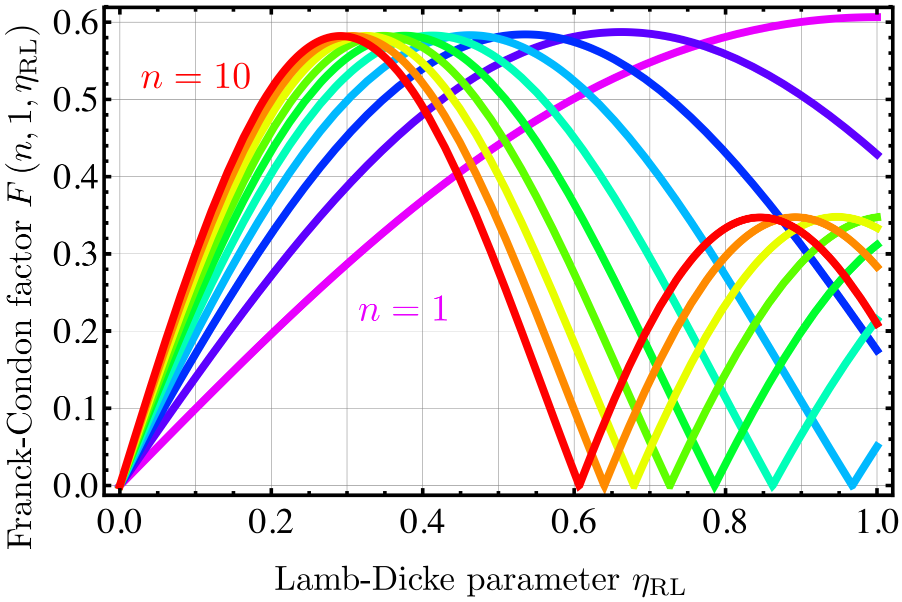

Figure 4.3: Franck-Condon factors from $n = 1$ to $n = 10$, $\Delta n = 1$ for Lamb-Dicke parameter between 0 and 1.

4.2 Theory of stimulated Raman transitions

Cooling has not been realized in the radial directions yet. Shifting the lattices associated to the two hyperfine states with respect to each other cannot be used in this case and sideband transitions cannot be driven with microwaves as described in Section 4.1. I will show that Raman transitions offer a solution to this problem.

4.2.1 Raman transitions in an ideal three level system

In the following I will start with a theoretical introduction to Raman transitions in an ideal three level system which is shown in Figure 4.4. The aim of the Raman transitions is to couple the two state $|\downarrow\rangle$ and $|\uparrow\rangle$ via an auxiliary state $|3\rangle$, respectively. Here $\varDelta$ denotes the detuning of the light fields coupling $|\downarrow\rangle$ and $|\uparrow\rangle$ to state $|3\rangle$ which is also called single photon detuning. $\varOmega_S$ and $\varOmega_P$ denote the Rabi frequencies for corresponding transition. δ is called two photon detuning and describes the detuning of the difference between the light fields $\varOmega_P$ and $\varOmega_S$ from the transition between $|\downarrow\rangle$ and $|\uparrow\rangle$.
The Raman process can be described as follows:
The system initially in the state $|\downarrow\rangle$ absorbs a photon out of the pump laser field. Thus the system is brought into a virtual intermediate state detuned by $\varDelta$ from state $|3\rangle$. By stimulated emission into the Stokes laser field the system passes over to state $|\uparrow\rangle$. This is a coherent process and works in either directions. It will lead to oscillations between state $|\downarrow\rangle$ and state $|\uparrow\rangle$ and if the detuning $\varDelta$ is sufficiently large, the probability to find the

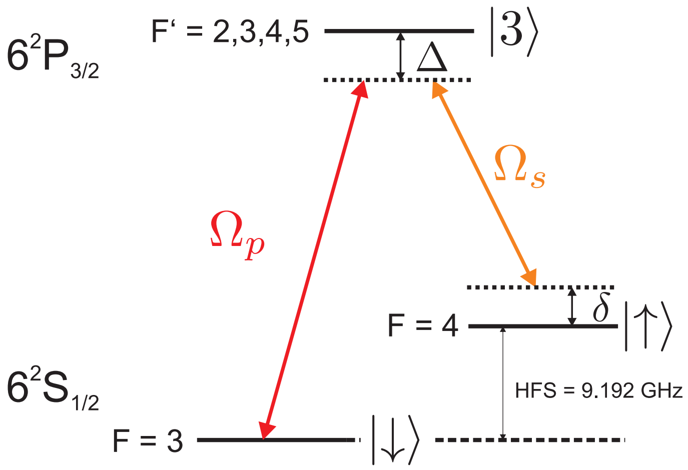

Figure 4.4: Simplified three level system.

system in the state $|3\rangle$ can be considered negligible; in this approximation the three level system reduces to an effective two level system. The characteristic variable describing this system is the Raman Rabi frequency Ω_R given by [35]:

$$\Omega_R = \frac{\Omega_S \cdot \Omega_P}{2\Delta} \tag{4.8}$$

if the two photon detuning is zero.

4.2.2 Magnetic substates of the hyperfine structure

The previous description assumed a pure three level system, I will now go into more detail and explain the effect of the different hyperfine states. The Rabi frequencies Ω_P and Ω_S, as used above, depend on the precise final and initial state as well as the polarization of the light field. The transitions have to fulfill the selection rules and hence Ω_P and Ω_S have to be replaced by a state dependent Rabi frequency:

$$\Omega_{F,m\rightarrow F',m'} = \frac{\langle F',m'|\,\hat{d}\cdot\hat{E}\,|F,m\rangle}{\hbar}. \tag{4.9}$$

Quantum mechanically several trajectories involving different intermediate excited states are possible and they all have to be accounted for by summing their probability amplitudes. The matrix element necessary to calculate the Rabi frequency can be reduced to algebraic functions and a single constant using the Wigner-Eckard theorem. The prefactors are closely related to Clebsch-Gordan coefficients and can be written using 3-j and 6-j symbols

[33].

$$\langle F',m'|\, er_q \cdot \hat{E}\, |F,m\rangle = (-1)^{2F'+J+I_C+m} \sqrt{(2F'+1)\,(2F+1)\,(2J+1)} \cdot \begin{pmatrix} 1 & F' & F \\ -q & m' & m' \end{pmatrix} \tag{4.10}$$

The remaining dipole matrix element $\langle J' = 3/2|\, |er_q|\, |J = 1/2\rangle$ generalized for the D_2 transition is related to the lifetime and the measured value is $(3.8014 \pm 0.0068) \cdot 10^{-29}\,\mathrm{C\,m}$ [33]. This formula guaranties also that selection rules for single transitions are fulfilled. The transitions with $\{\Delta m = 0, \Delta m = +1, \Delta m = -1\}$ will be also called $\{\pi,\sigma^+,\sigma^-\}$ transitions. The polarization of the light will determine which of these transitions will be driven.

4.3 Cooling scheme

Cooling along the axial direction has been realized using microwave radiation as discussed in Section 4.1. To cool atoms in the radial direction we need to have a Δk between the Rabi and Stokes laser beams which has a component along the radial direction. Having just one Δk would not be enough because this would only cool along the axis introduced by the vector. Hence I plan to use two Stokes beams and one pump beam to have two different Δk pointing to different directions in the radial plane.

Existing optics and coils for the magnetic fields limit the optical access to the atoms. Thus the decision was made to overlap the Raman laser beams with the laser beams for the MOT. This also forces the polarization of the beams to be circular. See Figure 4.5 for a schematic illustration. For the Raman transitions the polarization of the light in the reference frame defined by the quantization axis is relevant. The laser beams for the MOT define my initial coordinate system, with the beams along the x,y and z-axes (see Figure 4.5). This coordinate system uses the three unprimed unit vectors e_x,e_y,e_z. The coordinate system defined by the quantization axis is rotated by 45° around the z-axis with respect to the previous. The unit vectors of the coordinate system are primed and are given by $e'_x = \frac{e_x+e_y}{\sqrt{2}}$, $e'_y = \frac{e_x-e_y}{\sqrt{2}}$, $e'_z = e_z$. The pump light is entering the setup along the z-axis (e_z) and the stokes light along the x- (e_x) and y-axis (e_y) and are all circular polarized. The normalized light fields in the coordinate system defined by the quantization

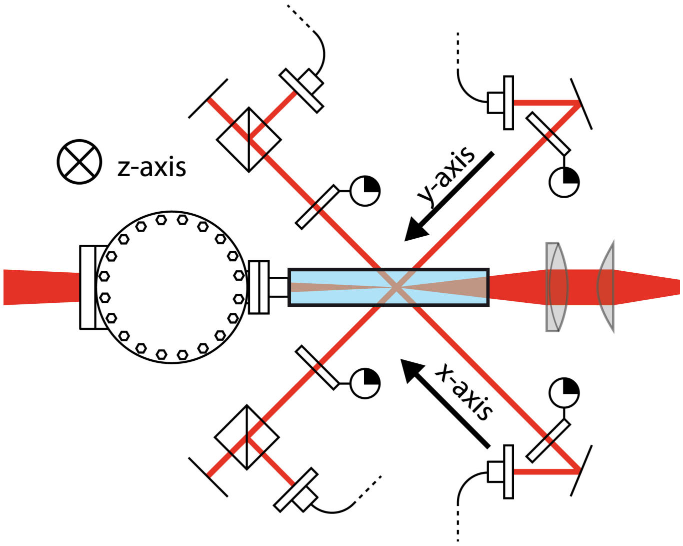

Figure 4.5: Optical access for Raman laser beams: Taking care of the right polarization the Raman laser beams are superimposed with the MOT beams on a polarizing beam splitter. This illustration shows two of the three MOT beams on which the stokes beams will be coupled to. The direction of the beams defines the x and y-axis as indicated by the arrows. The pump beam will be coupled in the same way to the third MOT beam which is perpendicular to the drawing surface. It defines the direction of the z-axis. The origin of the coordinate system is at the crossing point of all three MOT beams.

axis are:

$$\begin{aligned}
E_z =& E_0 e^{-ik_P z} e^{-i\omega_P t} \frac{1}{\sqrt{2}} \left(e_x - ie_y\right) \\
=& E_0 e^{-ik_p z} e^{-i\omega_p t} \frac{1}{\sqrt{2}} \left(e'_x - \frac{i}{2}\left(\left(e'_y + ie'_z\right) + \left(e'_y - ie'_z\right)\right)\right) \\
E_x =& E_0 e^{-ik_S x} e^{-i\omega_S t} \frac{1}{\sqrt{2}} \left(e_y - ie_z\right) \\
=& E_0 e^{-ik_S x} e^{-i\omega_S t} \left(\frac{1}{2}e'_x + \left(-\frac{1}{2\sqrt{2}} - \frac{1}{4}\right)\left(e'_y + ie'_z\right) + \left(\frac{1}{2\sqrt{2}} - \frac{1}{4}\right)\left(e'_y - ie'_z\right)\right) \\
E_y =& E_0 e^{-ik_S y} e^{-i\omega_S t} \frac{1}{\sqrt{2}} \left(e_z - ie_x\right) \\
=& E_0 e^{-ik_S y} e^{-i\omega_S t} \left(\frac{1}{2}e'_x + \left(-\frac{i}{2\sqrt{2}} - \frac{i}{4}\right)\left(e'_y + ie'_z\right) + \left(-\frac{i}{2\sqrt{2}} + \frac{i}{4}\right)\left(e'_y - ie'_z\right)\right).
\end{aligned}$$

The final coordinate system is chosen because the electric field oscillating along e'_x drives π transitions. The electric field oscillating along $\frac{1}{\sqrt{2}}\left(e'_y + ie'_z\right)$ ($\frac{1}{\sqrt{2}}\left(e'_y - ie'_z\right)$) drives σ^+ (σ^-) transitions, respectively. The amplitude of the Stokes light driving π is always the same, but the component driving σ^+ or σ^- depends on the axis and the polarization of the Stokes light. For the cooling scheme proposed here, the component driving σ^- transitions is not needed but the components driving σ^+ and π transitions. The MOT beams coming from different directions have different circular polarizations and thus one beam of the Stokes light has to enter from the side of the fiber coupler and the other from the side of the back reflecting mirror. Otherwise the Rabi frequency will be reduced by a factor of approximately 3.

There are two transitions involving different intermediate state which are not forbidden and have to be considered: $|\uparrow\rangle \leftrightarrow |F' = 4, m' = 4\rangle \leftrightarrow |\downarrow\rangle$ and $|\uparrow\rangle \leftrightarrow |F' = 4, m' = 3\rangle \leftrightarrow |\downarrow\rangle$. The first is driven by a π transition of the Stokes light and σ^+ transition of the pump light. For the second transition it is the other way around. These two paths interfere constructively. The effective Rabi frequency for no two photon detuning and an efficiency of η_{OPLL} for the phase lock between both lasers (see Chapter 4) is given by:

$$\Omega_{\mathrm{eff}} = \eta_{\mathrm{OPLL}} \cdot \frac{\sqrt{7}}{6} \frac{E_S \cdot E_P \left\langle J = 3/2 \right| |er| \left| J = 1/2 \right\rangle}{\hbar \cdot 2 \cdot \Delta \cdot 2\pi}. \tag{4.11}$$

The complete cooling cycle is displayed in Figure 4.6. The two pairs of Raman lasers are tuned to the first blue sideband and pump the atom from $|\uparrow, n\rangle$ to $|\downarrow, n-1\rangle$ and at the same time lower the vibrational state by one. The blue sideband is used to reduce the vibrational quantum number by 1 as the cooling start from the energetic higher state. The repumper laser pumps the atom up to the $|F' = 4, n-1\rangle$ state. From there it can decay spontaneous back to $|\uparrow, n-1\rangle$. The probability that the spontaneous emission or repumper laser changes the vibrational state is suppressed in the Lamb-Dicke regime. This requires that the energy difference between two vibrational states ΔE is higher than the recoil energy ($E_{\mathrm{rec}} = \hbar \cdot 2\pi \cdot 2\,\mathrm{kHz}$) resulting in a Lamb-Dicke parameter $\eta = \sqrt{\frac{\Delta E}{E_{\mathrm{rec}}}}$ smaller than 1. The state $|\uparrow, n = 0\rangle$ is a dark state because it does not couple to the Raman laser as well as to the repumper. Thus all atoms will stay in this state and the cooling cycle automatically stops assuming that there are no losses.

The Rabi frequency of the repumper beam should be twice the Raman Rabi frequency for the sideband transition. If the scattering rate is higher the atoms would always stay in their initial state due to the quantum Zeno effect and if the rate is lower the cooling process will last longer.

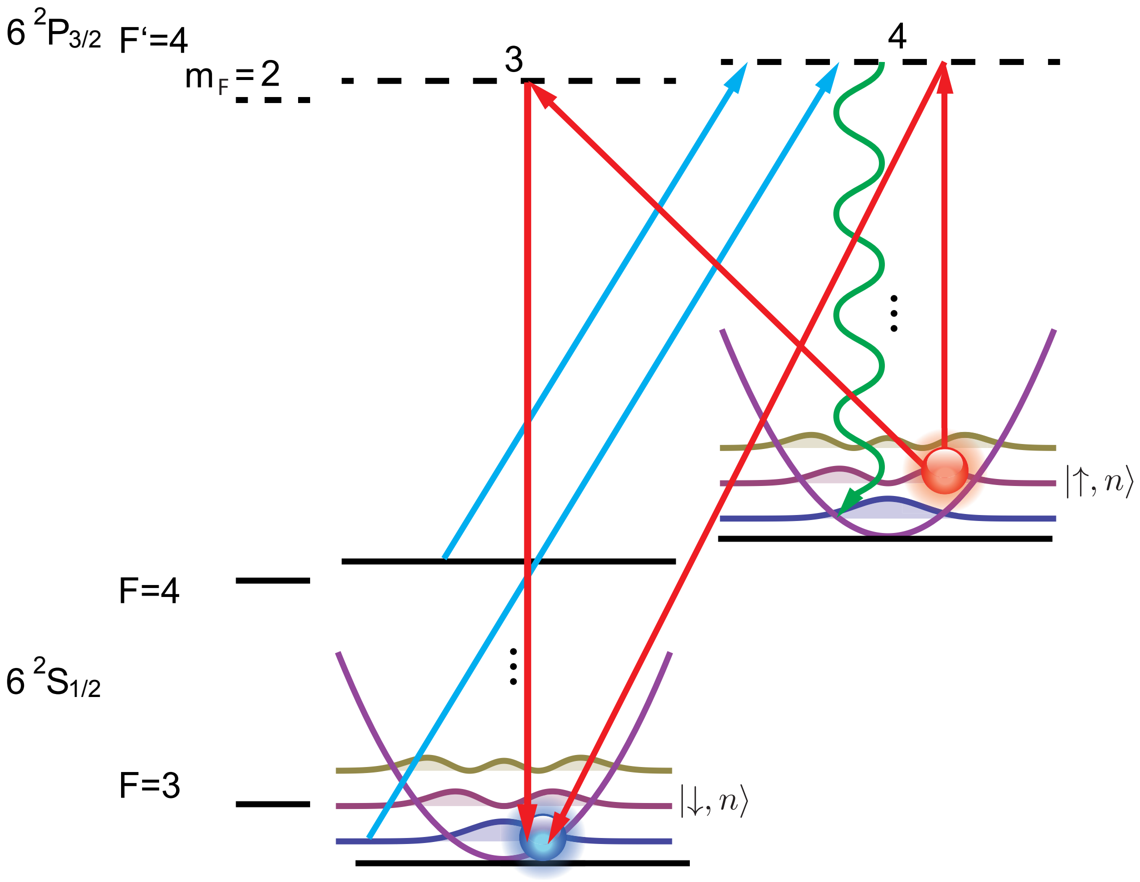

Figure 4.6: Resolved Raman sideband cooling scheme: The cooling cycle starts in the $|\uparrow\rangle$ state. The Raman laser beams (red) transfer atoms from $|\uparrow, n\rangle$ to $|\downarrow, n-1\rangle$ via two intermediate states. These two paths interfere constructively. The blue sideband is used to reduce the vibrational quantum number by 1 as the cooling start from the energetic higher state. The repumper laser (blue) pumps the atom up to the $|F' = 4, n-1\rangle$ state. From there it can decay spontaneous back to $|\uparrow, n-1\rangle$ (green). The second repumper laser (blue) pumps the atoms back to the cooling cycle which decay to the $|F = 4, m_F = 3\rangle$ state.

4.4 Optical phase lock loop

To drive coherent Raman transitions two, phase coherent light fields are needed. This can be accomplished with an optical phase locked loop (OPLL). In general, a phase locked loop compares the phase between two oscillators and controls the phase of one of these oscillators (slave) such that the oscillator has a fixed phase relation to the other one (master). The frequencies and electric field amplitudes of the two lasers will be labels with m and s, respectively. For an optical phase locked loop the two oscillators are lasers. The optical phase of the slave laser will be stabilized to a reference phase given by the master laser, which is free running in this setup. The two lasers are focused and superimposed on a fast photo diode. The beam size is optimized for the size of the photo diode. The beat note between both lasers is measure and used to adjust the phase difference between both lasers. With both beams having the same polarization the photo diode detects the following signal:

$$\begin{aligned} I_{PD} \propto & \left| E_m \cos\left(\omega_m t + \phi_m\right) + E_s \cos\left(\omega_s t + \phi_s\right)\right|^2 \\ = & \left|E_m\right|^2 \cos^2\left(\omega_m t + \phi_m\right) + \left|E_s\right|^2 \cos^2\left(\omega_s t + \phi_s\right) \\ & + 2E_m E_s \cos\left(\omega_m t + \phi_m\right) \cos\left(\omega_s t + \phi_s\right) \\ = & E_m E_s \cos\left(\left(\omega_m - \omega_s\right) t + \phi_m - \phi_s\right) \\ & + E_m E_s \cos\left(\left(\omega_m + \omega_s\right) t + \phi_m + \phi_s\right) \\ & + \left|E_m\right|^2 \cos^2\left(\omega_m t + \phi_m\right) + \left|E_s\right|^2 \cos^2\left(\omega_s t + \phi_s\right) . \end{aligned} \tag{4.12}$$

With the right experimental setup the term proportional to $\cos\left(\left(\omega_m - \omega_s\right) t + \phi_m - \phi_s\right)$ can be selected. The signal at this position will be called beat signal and is given by:

$$B(t) = A \cdot \cos\left(\left(\omega_m - \omega_s\right) t + \phi_m - \phi_s\right) . \tag{4.13}$$

An error signal proportional the phase difference $\phi_m - \phi_s$ can be generated by mixing this signal with a reference frequency of a local oscillator (LO). This generates a term proportional to the sum of the frequencies and a term proportional to the difference of the frequencies. After suppression of the term proportional to the sum frequency, by low-pass filtering, the error signal is given as:

$$\text{Error}(t) \propto \cos\left(\left(\omega_m - \omega_s - \omega_{LO}\right) t + \phi_m - \phi_s - \phi_{lo}\right) . \tag{4.14}$$

This signal simplifies for the case that the frequency of the LO is exactly the same as the frequency difference between the two lasers. Additionally one of the three phases, here the phase of the LO, can be fixed without loss of generality. If $\phi_{lo} = \frac{\pi}{2}$ is chosen the error signal becomes:

$$\text{Error}(t) \propto \sin\left(\phi_m - \phi_s\right) . \tag{4.15}$$

In a first order expansion this signal is linear in the phase difference between both lasers. The error signal is fed back to the slave laser to close the servo loop. This expansion is valid to describe the system, as the phase difference in a closed PLL is supposed to be zero.

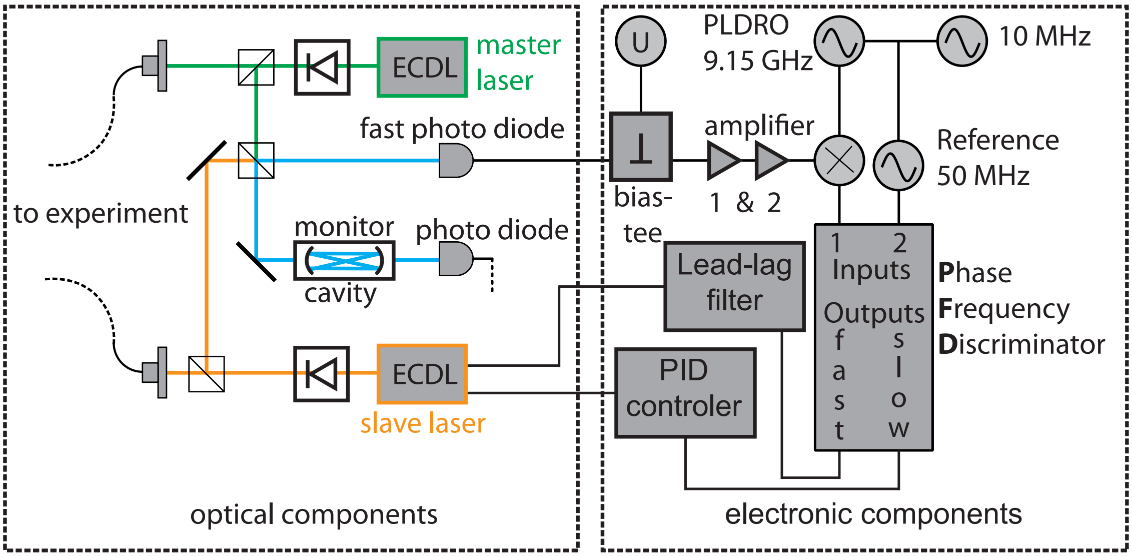
master laser
ECDL
fast photo diode
to experiment
monitor
cavity
photo diode
ECDL
slave laser
optical components
U
PLDRO
9.15 GHz
10 MHz
amplifier
1 & 2
bias-tee
Reference
50 MHz
Lead-lag filter
1 2
Inputs
Outputs
fast
slow
Phase Frequency Discriminator
PID controler
electronic components

Figure 4.7: Setup of the optical phase lock loop: Left half: The two external cavity diode lasers (ECDL) are each protected by an optical isolator. These two laser, labeled master and slave, are overlapped on a beam splitter. The lasers are monitored by a cavity. The beat note between both lasers is measured by a ultra fast photo diode. Right half: The photo diode is connected to a bias-tee supplying the optimal bias voltage. The RF signal out of the bias-tee is amplified and thereafter mixed down to 50 MHz with the 9.15 GHz signal provided by a PLDRO. The PFD compares this signal to the LO. The LO and the PLDRO are locked to a 10 MHz reference clock. The loop is closed with a PID controller connected to the piezoelectric ceramic acting on the grating of the slave laser and a lead-lag filter connected to the current input of the slave laser to shape the frequency response of the lock.

4.5 Experimental setup

In the actual setup the the realization of the OPLL is more advanced and contains more components than the basic OPLL discussed above (see Figure 4.7). The beat signal is mixed with a LO. The local oscillator will be labeled $LO1$ and it is realized by a phase-locked dielectric resonator oscillator (PLDRO) with a frequency of 9.15 GHz in the experiment. It is phase-locked to a rubidium reference clock by a 10 MHz signal. A term with the sum of the frequencies and a term with the difference of the frequencies is generated. The term with the sum of the frequencies is filtered out by the finite bandwidth of the electronics. The resulting signal oscillates at a frequency around 50 MHz rather than 9.2 GHz and will be called mixed down beat signal.

Instead of directly mixing this signal with a second LO, a phase frequency discriminator (PFD) compares the mixed down signal to the reference signal from LO. One advantage of a dedicated PFD chip is that the error signal is proportional to the phase difference and not only in first order approximation. More importantly, advanced chips offer also the ability to provide an error signal contingent on the frequency difference if the two input frequencies vary so much that the corresponding phase difference increases rapidly.

The feedback to the slave laser is realized via two paths. The slow feedback loop counteracts fluctuations in the bandwidth of 1 kHz covering an amplitude of a few hundred megahertz. This is realized with a piezoelectric ceramic controlling the grating of the external cavity diode laser via a PID servo loop. Fluctuations at higher bandwidth up to 3 MHz and smaller amplitudes less than 1 MHz are suppressed by modulation of the laser diode current. This fast feedback loop contains a lead-lag filter to shape the frequency characteristics of the error signal and was designed by K. Schörner. It ensures that the gain is small 1 for frequencies where the total phase shift is higher than 120° [36].

This OPLL locks the frequency difference between the master and slave laser to the sum of the PLDRO and LO frequencies (ω_{PLDRO}, ω_{LO}). The frequency $\omega_{PLDRO} + \omega_{LO}$ corresponds to the frequency ω_{LO} in Equation 4.14. The frequency of the PLDRO is fixed, but the frequency of the LO can be adjusted such that the frequency difference between both lasers can be tuned to meet the required frequency for the Raman transitions described in Section 4.2.

I list and explain here the main components used to realize an OPLL as shown in Figure 4.7. The heart of the electronic setup, the phase frequency detector, is explained in Section 4.5.1 in more detail.

Diode laser The two diode lasers are temperature stabilized external cavity diode lasers. These diode lasers are self made and the external cavity is terminated on one side by the diode itself and on the other side by a grating in Littrow configuration as described in [37]. The output wavelength can be tuned over roughly 2 nm (with mode hops) around the a center wavelength of 852 nm. This tuning can be realized by manually tilting the grating, changing the temperature of the whole diode laser and changing the current. To achieve tuning over a wide range during operation the grating can be also tilted using a piezoelectric crystal. This can tune the laser mode-hop free over a several hundred megahertz at a bandwidth of less than 1 kHz. Additionally the current of the laser can be modulated to achieve a tuning bandwidth of few megahertz over a smaller tuning range of up to 1 MHz.

Fast photo diode A ultra-fast photo diode is used to measure the beat note between both lasers at a frequency around 9.2 GHz. This photo diode is a Hamamatsu G4176-03. It has a typical sensitivity of $0.3\,\frac{\mathrm{A}}{\mathrm{W}}$ at 850 nm and an effective sensitive area of 0.2 mm × 0.2 mm. The responds time of the photo diode is 30 ps. A Mini-Circuits® ZX85-12G+ bias tee is used to provide the optimal bias voltage. The photo diode, the power supply of the photo diode and the further electronics are connected to the combined DC+RF, the individual DC and individual RF connector of the bias tee, respectively. This guarantees that the signal after the photo diode contains only the beat signal and no DC offset.

Amplifier The signal after the bias tee is too weak to be used by the phase frequency discriminator and thus two amplifiers are used. The first amplifier is the low noise amplifier Kuhne Electronics KU LNA 922A which has a gain of 25 dB at 9.2 GHz and just a bandwidth of 20 MHz. This acts directly as a band pass filter to reduce noise. The second amplifier is a Miteq AFS5-08001200-40-10P-5 which has a gain of 32 dB between 8 and 12 GHz.

Phase-locked dielectric resonator oscillator The Phase-Locked Dielectric Resonator Oscillator (PLDRO) serves to mix down the beat note. For this experiment a PLDRO manufactured by Resotech Inc. is used. It has a frequency of 9.15 GHz and is phase-locked to a reference frequency of 10 MHz from a rubidium reference clock. A spectrum analyzer phase-locked to the same reference shows a monochromatic signal with the resolution bandwidth of 1 Hz.

4.5.1 Phase frequency detector

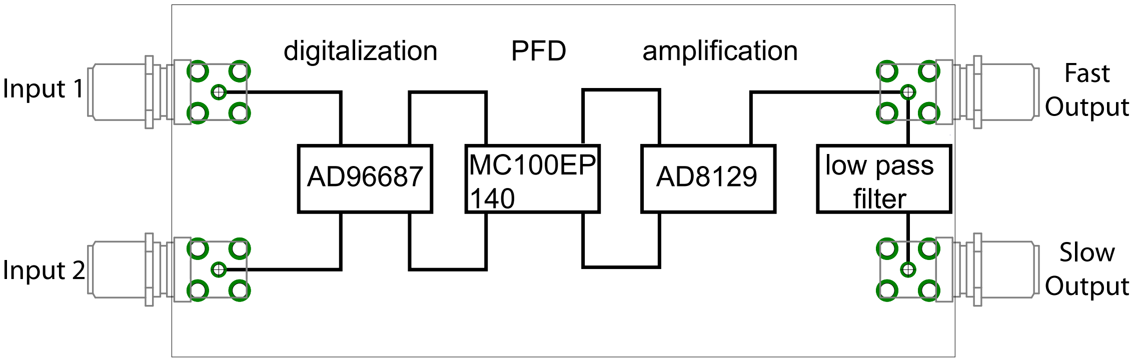

Figure 4.8: Simplified block diagram of the phase frequency detector board. The signals are first digitized by the comparator AD96687. The MC100EP140 is used as the phase frequency detector. The two output signals connected to the differential receiver amplifier AD8129. The fast output is directly connected to the output and the connection to the slow output includes a low pass filter. The complete circuit diagram provided by Professor Marco Prevedelli, Università di Bologna, can be found in the Appendix B.

The electronic setup of the phase frequency detector (PFD) is based on a design by Professor Marco Prevedelli (Università di Bologna) and its circuit diagram can be found in Appendix B. Figure 4.8 shows a simplified block diagram of the PFD circuit board. The purpose of this board is to compare two signals and generate an error signal proportional to the phase difference. If phase difference is larger than 2π the output saturates at either the maximum or minimum output voltage contingent on the sign of the phase difference. After the input of the circuit board the two signals are digitized by the ultrafast comparator AD96687. This chip can handle signals up to 500 MHz. Thereafter these ECL (emittercoupled logic) signals are analyzed by the phase frequency detector MC100EP140 which can work up to 2 GHz. Operating the chip at 5 V instead of 3.3 V increases the output voltages slightlyAND8040. It has two differential outputs which provide an error voltage after subtraction and integration. This integration and subtraction is done by frequency filters and the differential receiver amplifier AD8129 which has a common mode rejection ratio of 70 dB at 10 MHz. The amplification factor is controlled by passive elements and is configured to have a gain of 200 at zero-frequency decreasing at higher frequencies to 20 for a frequency of 4.5 MHz.

Measurements with two phase-locked signal generators with variable phase and frequency were used to test the circuit board. Figure 4.9 shows the signals at different positions on the board. With this configuration it was only possible to simulate constant phase or frequency differences. The PFD chip is specified with a transfer gain of 1.0mV/Degree at 1.4 GHz and 1.2mV/Degree at 1.0 GHz. This is amplified by 200 at zero-frequency and the output signal saturates for larger phase differences.

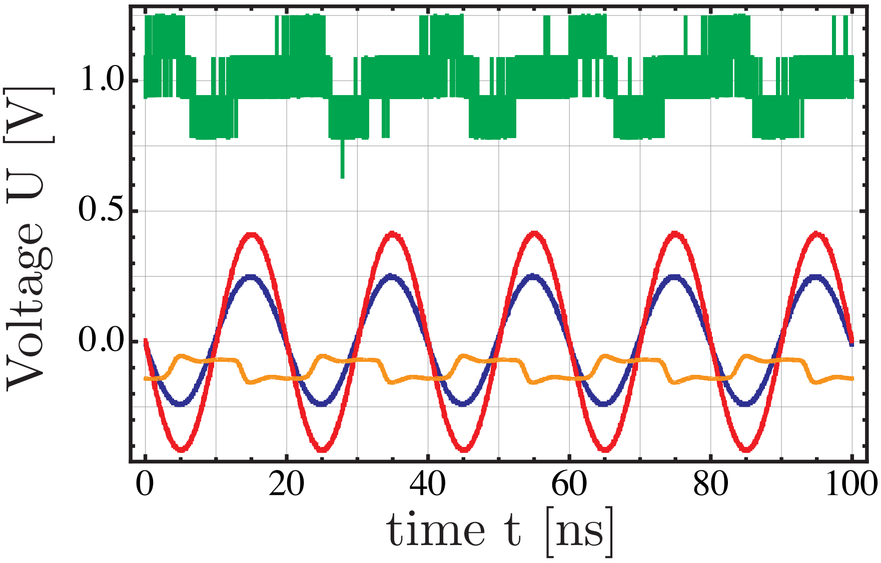

Figure 4.9: Phase frequency discriminator signals: Red and blue are the two sinusoidal input frequencies. Orange is one of the signals measured with a test probe between the PFD chip and the differential receiver amplifier. For this setting the signal is nearly the same amount of time in the lower state as in the higher state. The signal shape and hight is influenced by the test probe. Green is the signal at the fast output. The shape is dominated by digitalization noise of the oscilloscope. The signals for larger phase difference were recorded with the same setting and thus a large scaling had to be chosen for this channel. The ratio between the time of the orange signal in the upper state and the time in the lower state changes. Likewise the mean value of the output signal changes.

4.6 Characterization of the OPLL

4.6.1 Quadrature measurement

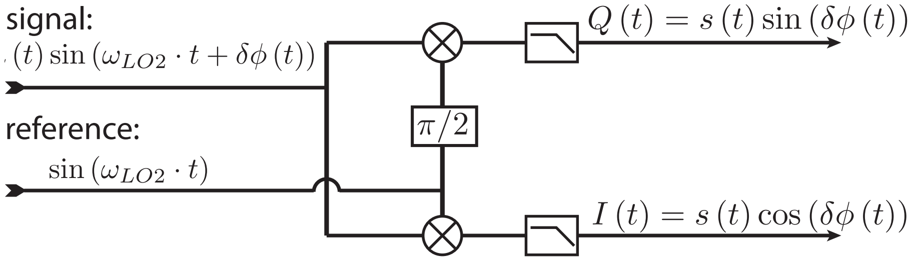
signal:
$(t)\sin\left(\omega_{LO2}\cdot t+\delta\phi\left(t\right)\right)$
reference:
$\sin\left(\omega_{LO2}\cdot t\right)$
$\pi/2$
$Q\left(t\right)=s\left(t\right)\sin\left(\delta\phi\left(t\right)\right)$
$I\left(t\right)=s\left(t\right)\cos\left(\delta\phi\left(t\right)\right)$

Figure 4.10: Schematic for quadrature measurement: The measured signal is mixed with the reference signal once directly and once with an additional phase delay of $\pi/2$ to obtain the in-phase and quadrature component of the measured signal.

The so-called quadrature signal of the beat signal between the Raman lasers provides a measurement of the phase fluctuations. For that, one has to split the down converted beat signal with amplitude $a\left(t\right)$, where one is mixed directly with the LO2 and the other with the LO2 with a phase offset of π. A BNC cable with the right length provides this phase shift. This corresponds to splitting the signal into a part oscillating as $\cos\left(\omega_{LO2}\right)$ with the amplitude $I\left(t\right)$ and into a part oscillating as $\sin\left(\omega_{LO2}\right)$ with the amplitude $Q\left(t\right)$. The schematics are shown in Figure 4.10.
Plotting the I signal versus the Q signal is a convenient way to visualize the amplitude of the signal and the phase with respect to the LO2. The amplitude of the original signal is given by $\left|a\left(t\right)\right|=\sqrt{I\left(t\right)^2+Q\left(t\right)^2}$, the radius from the origin. The phase is given by the azimuthal angle of the point described by the I and Q values. A signal with constant amplitude and fixed phase will be just a point in this coordinate system. Amplitude fluctuations will extend the point along the radial direction and phase fluctuations will extend the point along a circle around the origin.

The quadrature signals have to be low pass filtered for technical reasons. I used first order low pass filters with a cutoff frequency of 27 kHz. The data measured for my OPLL is visualized in Figure 4.11. The measured phase fluctuations are $\phi_{rms}=0.01\,\mathrm{rad}$.

4.6.2 Beat signal

My quadrature measurement was limited to determine fluctuations at frequencies less then 27 kHz, the cutoff frequency of the lowpass filter. The spectrum of beat signal provides another method to characterize the OPLL at higher frequencies. After the amplifiers, the optical beat signal is split with a power splitter and fed to spectrum analyzer. For a perfect OPLL this signal should be a monochromatic signal at sum of the 9.15 GHz coming from the PLDRO and the LO frequency used at the second input of the PFD

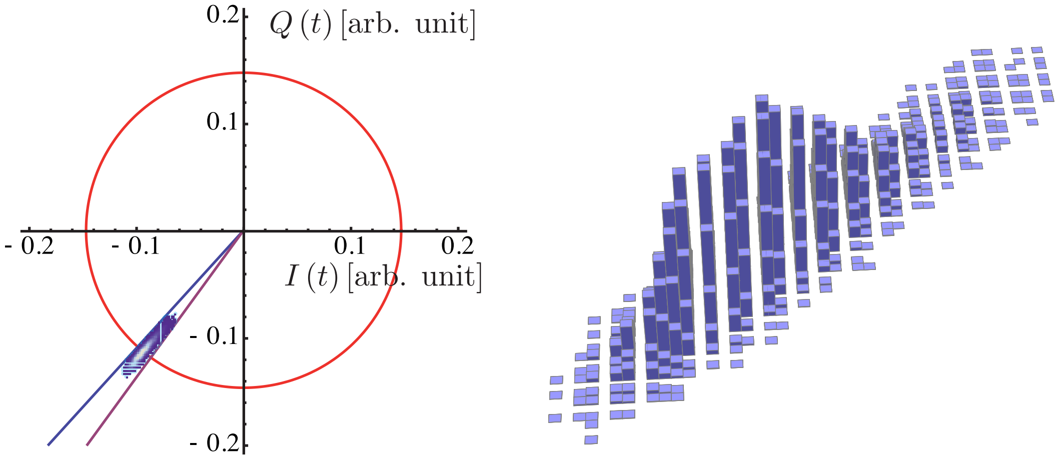

Figure 4.11: Quadrature measurement: Left: I and Q value of the signal plotted for 100 000 points. Right: 3D histogram of the measured points. The measurement yields a phase fluctuations of $\phi_{rms} = 0.01$ rad.

circuit board, which is set to 50 MHz for these tests. The signal will be broadened by phase or frequency fluctuations of the beat signal.

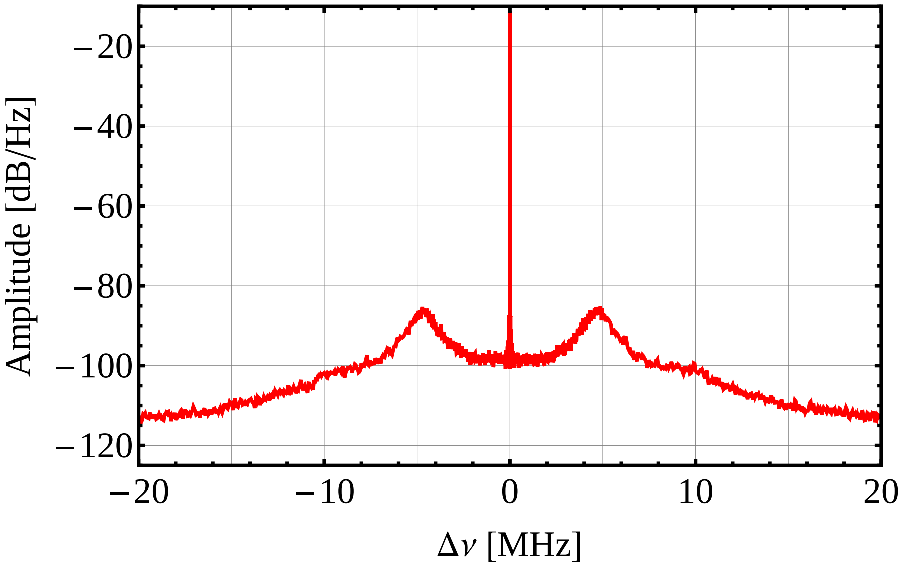

Figure 4.12: Spectrum of the optical phase lock loop signal: The center frequency is 9.2 GHz, servo bumps can be seen at ±4.8 MHz.

One figure of merit to characterize the phase stability of the system is the amount of power at the carrier frequency compared to the total power in the signal [38]. Several spectra with rough resolution bandwidth spanning a large frequency range down to spectra with fine resolution bandwidth and small frequency range are recorded and combined to get the whole spectrum with enhanced resolution at the beat frequency. The resolution bandwidth is 1 Hz (smallest as possible) at a frequency range of 50 Hz around the central frequency and the resolution bandwidth is 910 kHz at the edges of the spectrum with a total frequency range of 100 MHz. The central part of the spectrum with a range of 40 MHz is shown in Figure 4.12 and the deduced measurement values are given in Table 4.1.

frequency range	relative amount of power
Carrier (0 Hz)	93.5%
0- ± 54 kHz	0.02%
0- ± 1 MHz	0.2%
±8 MHz- ± 1 MHz	5.5%
>±8 MHz	0.8%

Table 4.1: Measured power distribution of the OPLL spectrum. This corresponds to a overall root mean square phase noise of 0.2 rad.

4.7 Measurements

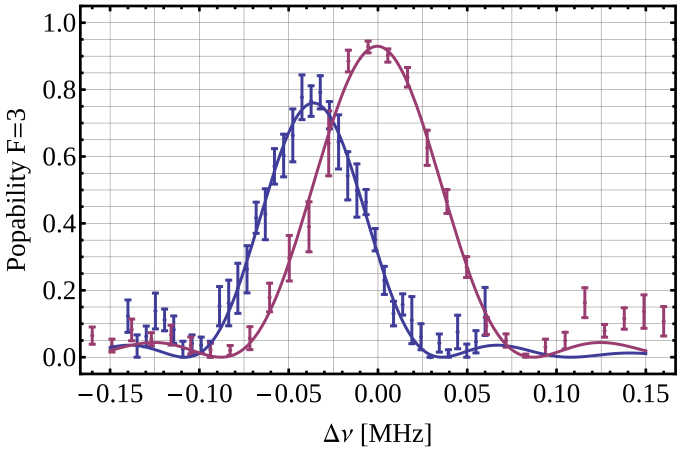

Figure 4.13: Raman and microwave spectrum: The microwave spectrum (red) has a height of 93 % and the center frequency is 9.199 84 GHz and is centered in this spectrum. The Raman spectrum (blue) has a height of 76 % ans the center frequency is 9.199 88 GHz.The frequency difference between both peaks is 40 kHz and is assigned to fluctuations of the setup over time.

The first calibration measurements were done with both Raman laser beams co-linear along the z-axis of the MOT beams. Having both beams in the same optical fiber guarantees perfect overlap but for this configuration no sidebands can be addressed since the transfered momentum is zero. The power of each laser beam was 500-600 µW and the beam waist $w(z)$ of the Gaussian beam at the position of the atoms was measured with a beam profile camera to be $w(z) = 210 \pm 10\,\mu\text{m}$. The single photon detuning was adjusted to 30 GHz and fluctuated over a day by up to 1 GHz. I measured the spectrum of the transition between $|\uparrow\rangle \leftrightarrow |\downarrow\rangle$ with the Raman laser beams and compared it with the spectrum taken with the microwave generator. After preparing the atoms in state $|\downarrow\rangle$ the laser beams were turned on for 14 µs. Afterwards the push-out is applied to remove all atoms in state $|\downarrow\rangle$ and the remaining atoms were counted. The frequency between the two Raman laser beams is scanned. For the microwave spectrum the same is done but with the microwave instead of the Raman laser. Both spectra are shown in Figure 4.13. The spectrum taken with the Raman laser beams has a slightly lower efficiency and is broader. Both measurements yield similar resonance frequencies of almost 9.2 GHz with a difference of 40 kHz. The difference between both spectra can be assigned to fluctuation of the setup over time. This differs from the well known 9.192 GHz for the hyperfine transition frequency of Cs atoms because an external magnetic field is applied to lift the degeneracy of the sub-states and because the Cs atoms are trapped in the lattice which induces a differential light shift.

4.7.1 Rabi oscillations

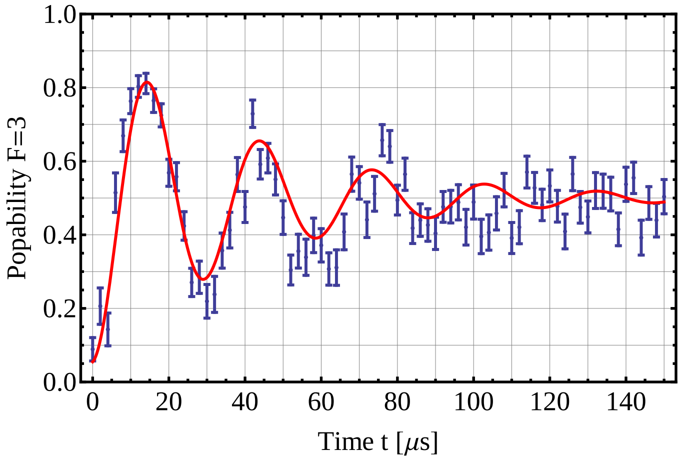

Figure 4.14: Rabi oscillation: The probability to find a atom in state $|\uparrow\rangle$ is measured for different times t for which the Raman laser illuminates the atoms. Equation 4.18 is fitted to the data. The results are presented in Table 4.2.

After the the resonance frequency is located, I want to test the capability of coherent interactions with the atoms. Therefore Rabi oscillations between the two spin states are measured. Starting with all atoms in state $|\downarrow\rangle$ the probability of atoms in state $|\uparrow\rangle$ will oscillate with the time t according to

$$P_{\uparrow}(t) = \frac{\Omega_0^2}{\Omega_{\text{eff}}^2} \sin^2\left(\frac{\Omega_{\text{eff}} t}{2}\right) \tag{4.16}$$

if no damping is assumed. I assume that the 90 % of the power is contained in the carrier of the OPLL. The resulting Rabi frequency is calculated with Equation 4.11 as follows:

$$\begin{aligned}\Omega_{\text{eff}} &= \eta_{\text{OPLL}} \cdot \frac{\sqrt{7}}{6} \frac{E_S \cdot E_P \left\langle J = 3/2 \right| |er| \left| J = 1/2 \right\rangle}{\hbar \cdot 2 \cdot \Delta \cdot 2\pi} \\ &= 2\pi \cdot 42\,\text{kHz} \\ E &= \sqrt{\frac{2I}{c\varepsilon_0}} \\ I(r=0) &= \frac{2P}{\pi\omega^2(z)} = \frac{2 \cdot 500\,\mu\text{W}}{\pi \cdot (210\,\mu\text{m})^2} = 14\,\text{mW}\ /\text{mm}^2\end{aligned} \tag{4.17}$$

The measured data (Figure 4.14) is fitted including damping which results from loss of coherence:

$$P_{\uparrow}(t) = \frac{1}{2}\left(1 - Ce^{\frac{t}{\tau}} \cos\left(\Omega_{\text{eff}} t\right)\right) \tag{4.18}$$

resulting in the data presented in Table 4.2. The reduced chi-square parameter of this fit is 2.9. The scattering rate of the Raman beams is 54 Hz. This cannot explain the short coherence time. Fluctuation of the dipole trap intensity can also be excluded because these would also affect analogously microwave induced coherent transitions. There a four times longer coherence time of was measured. Intensity fluctuations of the Raman laser at the relevant time scales can also be excluded because they should be visible in the spectrum of the beat signal.

A further effect which has not been considered so far is inhomogeneous dephasing due to inhomogeneous illumination. The two Raman laser beams have a Gaussian intensity distribution with $w(z) = 210 \pm 10\,\mu\text{m}$. The MOT loads Cs atoms into the optical lattice over a length of approximately 50 µm. At each lattice position the light intensity is different, resulting in different Rabi frequencies. The readout technique used during these sequences does not determine the location of the each atom. The recorded data is an average over

	Estimate	Standard error
Rabi frequency Ω_{eff}	$2\pi \cdot 33.8$ kHz	0.4 kHz
Contrast C	85 %	8 %
Coherence time τ	49 µs	8 µs

Table 4.2: Values obtained by fitting the measurement shown in Figure 4.14 with Equation 4.18.

all different Rabi frequencies. This effect can be numerically calculated assuming an equal distribution of atoms over the possible loading range and a perfect Gaussian intensity profile. The maximum of this beam does not have to be overlapped with the atoms central location, because the pointing of the Raman laser beams was adjusted to have a good overlap with the MOT beams which are five times larger. The measured data is fitted to this model using only the distance between the central position where atoms are loaded and the maximum of the Gaussian beam as a fit parameter. For this calculation the Rabi frequency calculated in Equation 4.17 is assumed and 100 equally spaced atoms positions are used to model the actual experimental situation. This results in a spacing of $\mathit{\Delta} x = 0.5\,\mu\text{m}$ between each position which is reasonable close to the actual spacing of $0.43\,\mu\text{m}$. This model has the following form:

$$P_{\uparrow}(t) = \frac{1}{2\cdot 100}\sum_{i=0}^{100}\left(1-\cos\left(\mathit{\Omega}_{\text{eff}}\, e^{\frac{2(x_0+(i-50)\cdot \mathit{\Delta} x)}{w(z)}}\, t\right)\right) \tag{4.19}$$

and the fit results in $x_0 = 75.6 \pm 1.2\,\mu\text{m}$ which means that the atom location does not reach the maximum of the Raman beam. The reduced chi-square is 1.1. The data with this fit is shown in Figure 4.15. This indicates that this model describe the data better than the model used above. It should be noted that the second model can explain the lower Rabi frequency and the contrast decay at the same time. The model is very simplified and for example assumes a perfect Gaussian beam. Dust on the glass cell could disturb the beam profile and would decrease the coherence length further. It also neglects all other decoherence effects. Larger Raman beams with higher intensity should increase the coherence time if the coherence time is limited by the inhomogeneous illumination investigated here.

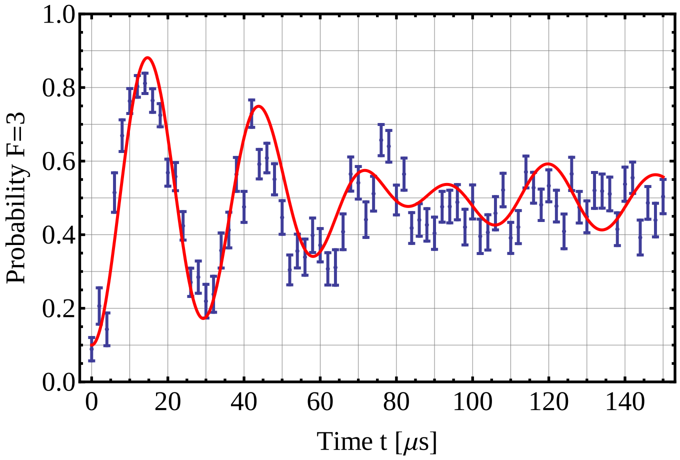

Figure 4.15: Model fitted to Rabi oscillations assuming Equation 4.19. The resulting misalignment of the Gaussian beam with respect to the center of the loading range is $x_0 = (75.6 \pm 1.2)\,\mu\text{m}$.

4.7.2 Ramsey oscillations

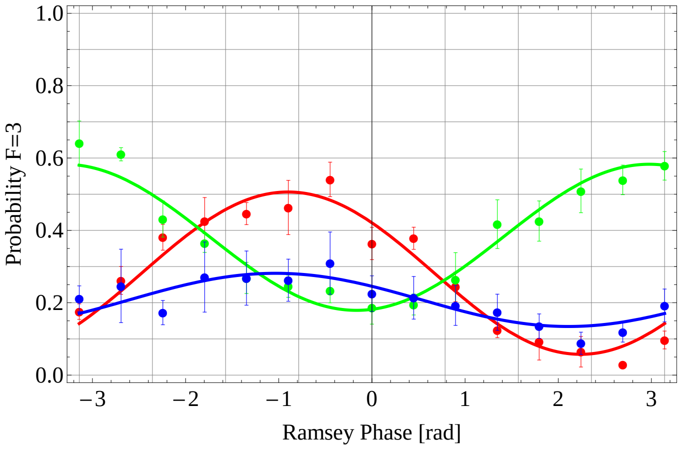

Figure 4.16: Ramsey fringes measured by changing the phase of the last $\pi/2$-pulse for three different waiting times t. Red: $t = 10\,\mu\text{s}$, green: $t = 110\,\mu\text{s}$, blue: $t = 200\,\mu\text{s}$.

Ramsey oscillations offer an alternative to measure the Rabi frequency and the coherence time. The simplest implementation uses two $\frac{\pi}{2}$ with a variable waiting time t between both pulses. The phase θ of the last $\frac{\pi}{2}$-pulse with respect to the first is scanned. This results again in a fringe following the form:

$$P_\uparrow(t) = \frac{1}{2}\left(1 + Ce^{-\frac{t}{\tau}}\sin\left(\phi(t) + \theta\right)\right). \tag{4.20}$$

Fringes are measured for varying waiting times (see Figure 4.16), and both the contrast $C(t)$ and the phase $\phi(t)$ are extracted. The phase and contrast evolution in time are shown in Figure 4.17. The phase is expected to follow $\phi(t) = \delta t$, with the two photon detuning δ, and the contrast should decay exponentially in time $C(t) = C_0 e^{\frac{t}{\tau}}$. The phase can be fitted perfectly but the statistics is not sufficient to fit the contrast with good videlity. The results are:

$$C_0 = (88 \pm 7)\,\% \qquad \tau = (634 \pm 486)\,\mu\text{s} \qquad \delta = 2\pi(13.9 \pm 0.3)\,\text{kHz}.$$

Any remaining inhomogeneous dephasing mechanisms can be suppressed by spin echo techniques. To eliminate time reversible effects, a π-pulse is applied exactly between the two $\frac{\pi}{2}$-pulses. However, more pulses will at the same time lead to more dephasing as shown with the Rabi oscillations in the last section, because they are effected by fluctuations of the Rabi frequency. The data taken to show this effect has to be interpreted with caution. Problems with the laser stability make the whole setup run unstable and it was not possible to reach the contrast of the measurements shown before. The spin echo technique shows that the contrast can be increased regardless of these problems. The

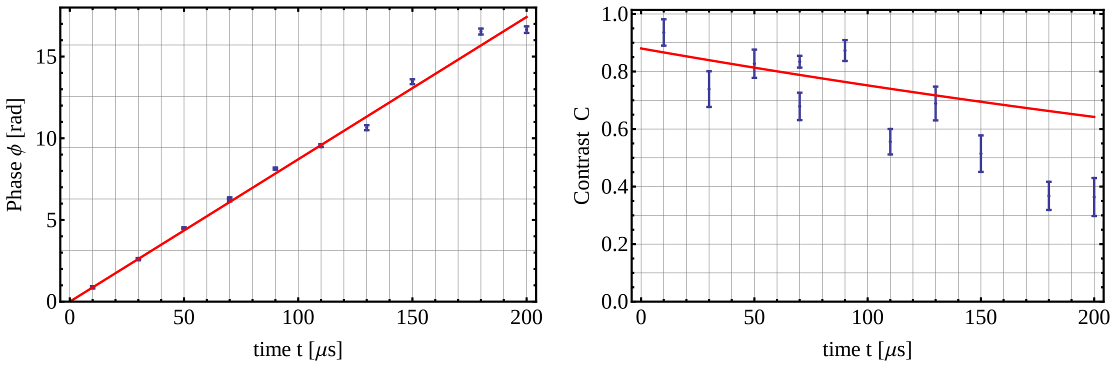

Figure 4.17: Left: Phase of the Ramsey fringe vs. time; Right: Contrast of the Ramsey fringe cs. time. The phase follows a linear increase with a slop of $\delta = 2\pi(13.9 \pm 0.3)\,\text{kHz}$ corresponding to the two photon detuning.

absolute increase was not determined because of these problems.

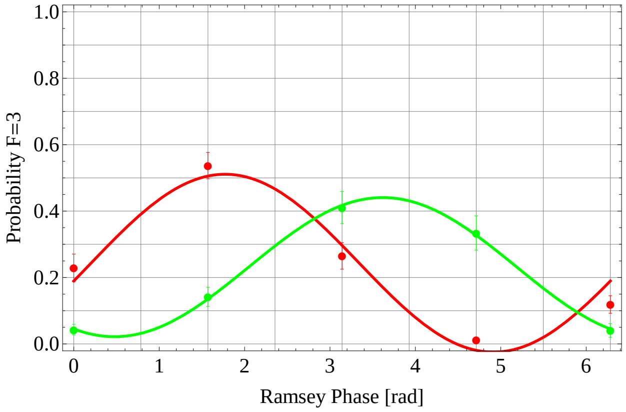

Figure 4.18: Ramsey fringes measured for a waiting time of $t = 200\,\mu\text{s}$ once with spin echo (green) and once without (red). The spin echo leads to a small increase in contrast.

5 Outlook

Experiments, conducted with the experimental setup I have worked with, are focused on single atom physics. Controlled interactions between two atoms open up new perspectives in the study of few body physics. In this thesis I have presented a model to estimate cold coherent collisions indicating that ground-state-cooled atoms are needed. A blue detuned doughnut shaped optical trap can increase the trapping frequencies in radial direction as I showed in an experiment. The suggested two arm setup will offer increased radial trapping frequencies and at the same time the state dependent transport can be realized. Two acousto-optic modulators will be used to control the intensity of both counter propagating Gaussian beams separately. In combination with the doughnut beam, this configuration will permit a greater flexibility in the control of the trapping frequencies independently. Controlling the trapping frequencies one can enable or suppress interaction and thus use this as a switch.

Increased trapping frequencies, realized with the doughnut shaped dipole trap, allow resolved sideband transitions and the Lamb-Dicke parameter will be approximately 0.3 with an expected trapping frequency of 20 kHz in radial direction. Both conditions are necessary to implement Raman side band cooling, leading to ground-state-cooled atoms in three dimensions combined with single atom control. In [24] it has been suggested that the dephasing in the single atom interferometer is mainly due to having thermal atoms. This effect is already reduced by axial ground-state-cooling and will be further reduced by radial ground-state-cooling.

Implementation of quantum computation algorithms have been realized with ions, lined up in a single trap [39]. Similar experiments are planned with Rydberg atoms [40]. Cold interaction between neutral atoms will lead to an additional alternative to realize quantum computation [41]. This system has a good scalability as it can be extended to two or even three dimensions. The ultimate goal is the realization of a system which fulfills all criteria proposed by David DiVincenzo for a quantum computer [42].

Cooling atoms in the ground-state will allow us to study the atom analog of the Hong-Ou-Mandel effect. This is a purely quantum mechanical effect of interference between two indistinguishable particles. As such the experiment requires that two cesium atoms can be prepared in exactly the same quantum state. A sequence realizing this experiment is shown in Figure 5.1. At the end of this sequence the atoms are either both at the left lattice site or at the right lattice site. The atoms are illuminated with resonant light

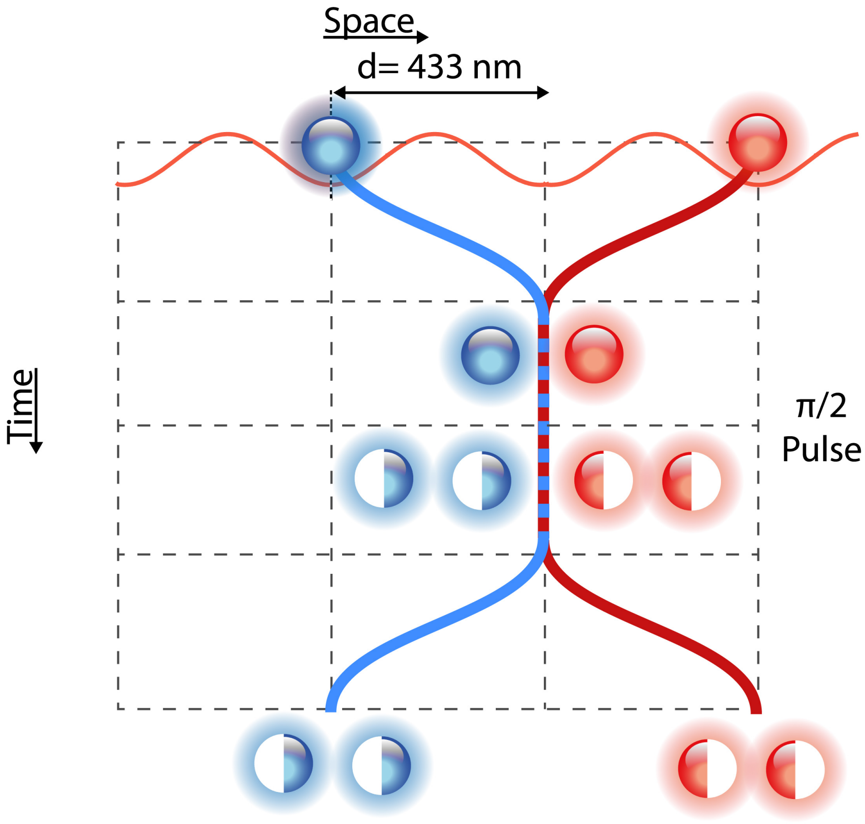

Figure 5.1: Hong-Ou-Mandel like sequence: Two atoms are overlapped at the same lattice site with the state dependent transport. Then a $\pi/2$ pulse is applied bringing both atoms in a super position of both states. There after the state dependent transport is applied in the opposite direction. At the end of the sequence both atoms are either at the left lattice site or on the right lattice site.

during the final picture. This light will lead to light induced collisions whereby both atoms are lost. The signature of the Hong-Ou-Mandel effect in this sequence would be that the atoms loss rate increases significantly. Unlike the classical Hong-Ou-Mandel experiment with photons we will be able to use interactions between both particles to modify the results.

Bibliography

[1] Peter W. Shor. Polynomial-time algorithms for prime factorization and discrete logarithms on a quantum computer. *SIAM Review*, 41(2):pp. 303–332, 1999.

[2] David P DiVincenzo. Topics in quantum computers. *cond-mat/9612126*, December 1996.

[3] Seth Lloyd. Almost any quantum logic gate is universal. *Phys. Rev. Lett.*, 75(2): 346–349, Jul 1995.

[4] Isaac L. Chuang, Neil Gershenfeld, and Mark Kubinec. Experimental implementation of fast quantum searching. *Phys. Rev. Lett.*, 80(15):3408–3411, Apr 1998.

[5] J. I. Cirac and P. Zoller. Quantum computations with cold trapped ions. *Phys. Rev. Lett.*, 74(20):4091–4094, May 1995.

[6] Thomas Monz, Philipp Schindler, Julio T. Barreiro, Michael Chwalla, Daniel Nigg, William A. Coish, Maximilian Harlander, Wolfgang Hänsel, Markus Hennrich, and Rainer Blatt. 14-qubit entanglement: Creation and coherence. *Phys. Rev. Lett.*, 106 (13):130506, Mar 2011.

[7] Alexander Shnirman, Gerd Schön, and Ziv Hermon. Quantum manipulations of small josephson junctions. *Phys. Rev. Lett.*, 79(12):2371–2374, Sep 1997.

[8] M. H. Anderson, J. R. Ensher, M. R. Matthews, C. E. Wieman, and E. A. Cornell. Observation of Bose-Einstein condensation in a dilute atomic vapor. *Science*, 269 (5221):198 –201, July 1995.

[9] T. Wilk, A. Gaëtan, C. Evellin, J. Wolters, Y. Miroshnychenko, P. Grangier, and A. Browaeys. Entanglement of two individual neutral atoms using rydberg blockade. *Phys. Rev. Lett.*, 104(1):010502, Jan 2010.

[10] D. Jaksch, H.-J. Briegel, J. I. Cirac, C. W. Gardiner, and P. Zoller. Entanglement of atoms via cold controlled collisions. *Phys. Rev. Lett.*, 82(9):1975–1978, Mar 1999.

[11] Olaf Mandel, Markus Greiner, Artur Widera, Tim Rom, Theodor W. Hansch, and Immanuel Bloch. Controlled collisions for multi-particle entanglement of optically trapped atoms. *Nature*, 425(6961):937–940, October 2003.

[12] Michał Karski, Leonid Förster, Jai-Min Choi, Wolfgang Alt, Andrea Alberti, Artur Widera, and Dieter Meschede. Direct observation and analysis of Spin-Dependent transport of single atoms in a 1D optical lattice. *arXiv:1102.3356*, February 2011.

[13] Michał Karski, Leonid Förster, Jai-Min Choi, Andreas Steffen, Wolfgang Alt, Dieter Meschede, and Artur Widera. Quantum walk in position space with single optically trapped atoms. *Science*, 325(5937):174 –177, July 2009.

[14] C. Monroe, D. M. Meekhof, B. E. King, S. R. Jefferts, W. M. Itano, D. J. Wineland, and P. Gould. Resolved-sideband raman cooling of a bound atom to the 3d zero-point energy. *Phys. Rev. Lett.*, 75(22):4011–4014, Nov 1995.

[15] S. E. Hamann, D. L. Haycock, G. Klose, P. H. Pax, I. H. Deutsch, and P. S. Jessen. Resolved-sideband raman cooling to the ground state of an optical lattice. *Phys. Rev. Lett.*, 80(19):4149–4152, May 1998.

[16] G. Lamporesi, A. Bertoldi, L. Cacciapuoti, M. Prevedelli, and G. M. Tino. Determination of the newtonian gravitational constant using atom interferometry. *Phys. Rev. Lett.*, 100(5):050801, Feb 2008.

[17] Rudolf Grimm, Matthias Weidemüller, and Yurii B Ovchinnikov. Optical dipole traps for neutral atoms. *physics/9902072*, February 1999. Advances in Atomic, Molecular and Optical Physics Vol. 42, 95-170 (2000).

[18] Xiaodong He, Peng Xu, Jin Wang, and Mingsheng Zhan. Combining red- and blue-detuned optical potentials to form a Lamb-Dicke trap for a single neutral atom. November 2010.

[19] E. R. I. Abraham, W. I. McAlexander, C. A. Sackett, and Randall G. Hulet. Spectroscopic determination of the s-wave scattering length of lithium. *Phys. Rev. Lett.*, 74: 1315–1318, Feb 1995.

[20] S. Inouye, M. R. Andrews, J. Stenger, H.-J. Miesner, D. M. Stamper-Kurn, and W. Ketterle. Observation of feshbach resonances in a Bose-Einstein condensate. *Nature*, 392(6672):151–154, March 1998.

[21] Franz Schwabl. *Quantenmechanik (QM I)*. Springer, Berlin, 6. a., korr. nachdr. 2004 edition, September 2004. ISBN 3540431063.

[22] Gernot Münster. *Quantentheorie (Gruyter - de Gruyter Lehrbücher)*. Gruyter, bilingual edition, February 2006. ISBN 3110189283.

[23] René Stock and Ivan H. Deutsch. Trap-induced resonances in controlled collisions of cesium atoms. *Physical Review A*, 73(3):032701, March 2006.

[24] Michał Karski. *State-selective transport of single neutral atoms*. PhD thesis, Rheinische Fridrich-Wilhelms-Universität Bonn, 2010.

[25] Markus Greiner, Olaf Mandel, Theodor W. Hänsch, and Immanuel Bloch. Collapse and revival of the matter wave field of a Bose-Einstein condensate. *Nature*, 419:51–54, September 2002.

[26] Leonid Förster, Michalstrok Karski, Jai-Min Choi, Andreas Steffen, Wolfgang Alt, Dieter Meschede, Artur Widera, Enrique Montano, Jae Hoon Lee, Worawarong Rakreungdet, and Poul S. Jessen. Microwave control of atomic motion in optical lattices. *Physical Review Letters*, 103(23):233001, December 2009.

[27] Förster Leonid. *Microwave control of atomic motion in a spin dependent optical lattice*. PhD thesis, Rheinische Fridrich-Wilhelms-Universität Bonn, 2010.

[28] M. Karski, L. Förster, J. M. Choi, W. Alt, A. Widera, and D. Meschede. Nearest-neighbor detection of atoms in a 1d optical lattice by fluorescence imaging. *Phys. Rev. Lett.*, 102(5):053001, Feb 2009.

[29] M. Padgett. An experiment to observe the intensity and phase structure of laguerre-gaussian laser modes. *American Journal of Physics*, 64(1):77, 1996.

[30] N. R. Heckenberg, R. McDuff, C. P. Smith, and A. G. White. Generation of optical phase singularities by computer-generated holograms. *Optics Letters*, 17(3):221–223, February 1992.

[31] Arif Marwadrdi. Generation of a donut beam for a tight radial confinement of atoms in a one-dimensional optical lattice. Master's thesis, Rheinische Fridrich-Wilhelms-Universität Bonn, 2010.

[32] Alt Wolfgang. Optical control of single neutral atoms. Master's thesis, Rheinische Fridrich-Wilhelms-Universität Bonn, 2004.

[33] D. A. Steck. Cesium d line data. *Department of Physics, The University of Texas at Austin, Austin, TX*, pages 78712–1081, 1998.

[34] D. J. Wineland and Wayne M. Itano. Laser cooling of atoms. *Phys. Rev. A*, 20(4): 1521–1540, Oct 1979.

[35] C. Monroe, D. M. Meekhof, B. E. King, S. R. Jefferts, W. M. Itano, D. J. Wineland, and P. Gould. Resolved-Sideband raman cooling of a bound atom to the 3D Zero-Point energy. *Physical Review Letters*, 75(22):4011, November 1995.

[36] Karsten Schörner. Ein phasenstabilisiertes lasersystem für resonatorinduzierte raman-prozesse. Master's thesis, Rheinische Fridrich-Wilhelms-Universität Bonn, 2008.

[37] L. Ricci, M. Weidemüller, T. Esslinger, A. Hemmerich, C. Zimmermann, V. Vuletic, W. König, and T.W. Hänsch. A compact grating-stabilized diode laser system for atomic physics. *Optics Communications*, 117(5-6):541–549, June 1995.

[38] Miao Zhu and John L. Hall. Stabilization of optical phase/frequency of a laser system: application to a commercial dye laser with an external stabilizer. *Journal of the Optical Society of America B*, 10(5):802–816, May 1993.

[39] H. Häffner, C.F. Roos, and R. Blatt. Quantum computing with trapped ions. *Physics Reports*, 469(4):155–203, December 2008.

[40] M. Saffman, T. G. Walker, and K. Mølmer. Quantum information with rydberg atoms. *Reviews of Modern Physics*, 82(3):2313, 2010.

[41] Anders Sørensen and Klaus Mølmer. Spin-Spin interaction and spin squeezing in an optical lattice. *Physical Review Letters*, 83(11):2274, 1999.

[42] David P DiVincenzo and IBM. The physical implementation of quantum computation. *arXiv:quant-ph/0002077*, February 2000.

List of Figures

2.1 Collision sequence 5
2.2 Overlap Integral 7
2.3 Simulated phase rate 8
2.4 Phase and contrast vs. $\bar{n}$ 10
2.5 Phase and contrast vs. interaction time 10

3.1 Experimental setup 12
3.2 Spiral phase plate 14
3.3 Beam profile of doughnut and Gaussian beam 16
3.4 Dependency of the tapered amplifier output power 17
3.5 Tapered amplifier collimation 18
3.6 Spectrum of the tapered amplifier 18
3.7 Integration of the doughnut beam 21
3.8 Two arm optical lattice 22
3.9 Propagation of the doughnut beam 23
3.10 Beat note between both dipole trap lasers 24
3.11 Atom size on the CCD camera 25

4.1 Level scheme including vibrational states 27
4.2 Microwave sideband cooling scheme 30
4.3 Franck-Condon factor 31
4.4 Simplified three level system. 32
4.5 Optical access for Raman laser beams 34
4.6 Resolved Raman sideband cooling scheme 36
4.7 Setup of the optical phase lock loop 38
4.8 Simplified phase frequency detector board block diagram 40
4.9 Phase frequency discriminator signals 41
4.10 Schematic for quadrature measurement 42
4.11 Quadrature measurement 43
4.12 Spectrum of the optical phase lock loop 43
4.13 Raman and microwave spectrum 44
4.14 Rabi oscillation 45
4.15 Model fitted to Rabi oscillations 47
4.16 Ramsey fringes 48
4.17 Ramsey contrast and phase vs. time 49

4.18 Ramsey fringe with and without spin echo 49
5.1 Hong-Pu-Mandel like sequence 52

List of Tables

3.1 Parameter present dipole trap 13
3.2 Specification of the dichroic mirror 20

4.1 Power distribution of the OPLL spectrum 44
4.2 Rabi oscillation values 46

A.1 Values of the overlap integral 62

A Further calculation of the overlap integral

The Integral $I_{n,m} = \int d\tilde{x} \left|\tilde{\psi}_1 \left(\widetilde{x,n}\right)\right|^2 \left|\tilde{\psi}_2 \left(\widetilde{x,m}\right)\right|^2$ also shown in Equation 2.11 can be further calculated to deduce that this integral is a product of a constant and a rational number which depends on the vibrational quantum numbers n and m. There for I write out the harmonic oscillator wavefunction using Hermite functions $H_n(x)$.

$$I_{n,m} = \int\limits_{-\infty}^{\infty} \frac{1}{\sqrt{\pi}2^n n!} e^{-x^2} \left(H_n(x)\right)^2 \frac{1}{\sqrt{\pi}2^m m!} e^{-x^2} \left(H_m(x)\right)^2 dx \tag{A.1}$$

$$= \frac{2}{\sqrt{\pi}2^n n! \sqrt{\pi}2^m m!} \int\limits_{0}^{\infty} e^{-2x^2} \left(H_n(x)\right)^2 \left(H_m(x)\right)^2 dx \tag{A.2}$$

I now carry out the substitution $y = 2x^2$:

$$I_{n,m} = \frac{2}{\sqrt{\pi}2^n n! \sqrt{\pi}2^m m!} \int\limits_{0}^{\infty} e^{-y} \left(H_n\left(\sqrt{\frac{y}{2}}\right)\right)^2 \left(H_m\left(\sqrt{\frac{y}{2}}\right)\right)^2 \frac{1}{\sqrt{2}} y^{-\frac{1}{2}} dy \tag{A.3}$$

$$\tag{A.4}$$

Here I can apply the identity for the product of two Hermite polynomials:

$$H_n(z) H_m(z) = n!m! \sum_{k=0}^{\min(n,m)} \frac{2^k H_{-2k+m+n}(z)}{k!\,(n-k)!\,(m-l)!} \tag{A.5}$$

This is applied to the to $\left(H_m\left(\sqrt{\frac{y}{2}}\right)\right)^2$ and $\left(H_n\left(\sqrt{\frac{y}{2}}\right)\right)^2$:

$$\begin{aligned} I_{n,m} =& \frac{\sqrt{2}}{\sqrt{\pi}2^n n! \sqrt{\pi}2^m m!} \int\limits_{0}^{\infty} e^{-y} y^{-\frac{1}{2}} \\ & \cdot n!^2 \sum_{k=0}^{n} \frac{2^k H_{2(n-k)}\left(\sqrt{\frac{y}{2}}\right)}{k!\left((n-k)!\right)^2} m!^2 \sum_{l=0}^{n} \frac{2^k H_{2(m-l)}\left(\sqrt{\frac{y}{2}}\right)}{l!\left((m-l)!\right)^2} dy \end{aligned} \tag{A.6}$$

I can now use the relation between Hermite polynomials and Laguerre polynomials $L_n^{\alpha}(x)$:

$$H_{2n}(x) = (-4)^n n! L_n^{-\frac{1}{2}}\left(x^2\right) \tag{A.7}$$

For now I will just consider the Integral and I will move the sums out of the integral:

$$\int_0^{\infty} e^{-y} y^{-\frac{1}{2}} L_{n-k}^{-\frac{1}{2}}\left(\frac{y}{2}\right) L_{m-l}^{-\frac{1}{2}}\left(\frac{y}{2}\right) dy \tag{A.8}$$

$$= \int_0^{\infty} e^{-y} y^{-\frac{1}{2}} \sum_{p=0}^{n-k} \binom{n-k-\frac{1}{2}}{n-k-p} \left(-\frac{1}{2}\right)^p \left(-\frac{3}{2}\right)^{n-k-p} L_p^{-\frac{1}{2}}(y) \tag{A.9}$$

$$\cdot \sum_{q=0}^{m-l} \binom{m-l-\frac{1}{2}}{m-l-q} \left(-\frac{1}{2}\right)^q \left(-\frac{3}{2}\right)^{m-l-q} L_q^{-\frac{1}{2}}(y) dy \tag{A.10}$$

For the last step I used the rule for multiple arguments:

$$L_n(z_1 \cdot z_2) = \sum_{k=0}^{n} \binom{n}{n-k} L_k(z_2) \tag{A.11}$$

Considering again only the integral the orthogonality relation can be applied:

$$\int_0^{\infty} dy e^{-y} y^{-\frac{1}{2}} L_p^{-\frac{1}{2}}(y) L_q^{-\frac{1}{2}}(y) dy = \frac{\Gamma\left(p+\frac{1}{2}\right)}{p!} \delta_{p,q} \tag{A.12}$$

$$= \frac{\frac{(2p)!}{p!4^p}\sqrt{\pi}}{p!} \delta_{p,q} \tag{A.13}$$

This shows that the final result can be written in terms of polynomials of n and m multiplied by a power of π. The first 4x4 values calculated with Mathematica can be found in Table A.1

	n=0	n=1	n=2	n=3
m=0	$\frac{1}{\sqrt{2\pi}}$	$\frac{1}{2}\frac{1}{\sqrt{2\pi}}$	$\frac{3}{8}\frac{1}{\sqrt{2\pi}}$	$\frac{5}{16}\frac{1}{\sqrt{2\pi}}$
m=1	$\frac{1}{2}\frac{1}{\sqrt{2\pi}}$	$\frac{3}{4}\frac{1}{\sqrt{2\pi}}$	$\frac{7}{16}\frac{1}{\sqrt{2\pi}}$	$\frac{11}{32}\frac{1}{\sqrt{2\pi}}$
m=2	$\frac{3}{8}\frac{1}{\sqrt{2\pi}}$	$\frac{7}{16}\frac{1}{\sqrt{2\pi}}$	$\frac{41}{64}\frac{1}{\sqrt{2\pi}}$	$\frac{51}{128}\frac{1}{\sqrt{2\pi}}$
m=3	$\frac{5}{16}\frac{1}{\sqrt{2\pi}}$	$\frac{11}{32}\frac{1}{\sqrt{2\pi}}$	$\frac{51}{128}\frac{1}{\sqrt{2\pi}}$	$\frac{147}{256}\frac{1}{\sqrt{2\pi}}$

Table A.1: Values of the overlap integral

B Phase frequency discriminator circuit diagram

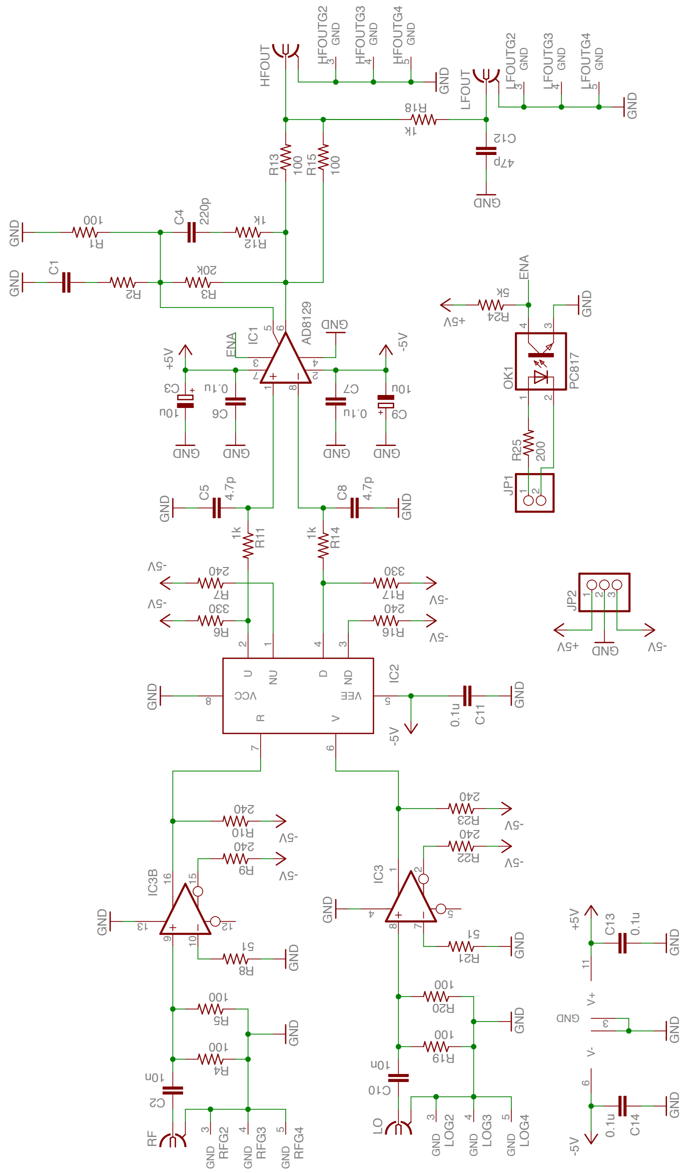
HFOUT
HFOUTG2
HFOUTG3
HFOUTG4
LFOUT
LFOUTG2
LFOUTG3
LFOUTG4
GND
R13 100
R15 100
R18 1k
C12 47p
R1 100
C4 220p
R12 1k
C1
R2
R3 20k
IC1
AD8129
ENA
+5V
-5V
C3 10u
C6 0.1u
C7 0.1u
C9 10u
C5 4.7p
C8 4.7p
R11 1k
R14 1k
R7 240
R6 330
R17 330
R16 240
IC2
U
NU
D
ND
VCC
VEE
R
V
C11 0.1u
R24 5K
OK1
PC817
R25 200
JP1
JP2
IC3B
IC3
R10 240
R9 240
R8 51
R5 100
R4 100
C2 10n
RF
RFG2
RFG3
RFG4
R23 240
R22 240
R21 51
R20 100
R19 100
C10 10n
LO
LOG2
LOG3
LOG4
C13 0.1u
C14 0.1u
V+
V-

Acknowledgments

At this point I want to thank everybody who supported me during my Bachelor and Master at the University of Bonn.

First of all I want to thank Prof. D. Meschede for giving me the opportunity to collaborate at a very interesting project. I know Prof. D. Meschede since the first days studding in Bonn and disposed be to do quantum optics.

I thank Prof. A. Widera to be my second referee. Moreover I want to give thank to Prof. A. Widera for his advice and the assistance he offered me during the time he worked in Bonn.

A special thanks goes to all members of the working group supporting me the whole time. I had a very pleasant time and enjoyed studying physics. Likewise, I enjoyed all extra activities with them. I just want to mention the daily tee break. It was very valuable to sit together and talk about all kind of topics frequently also not necessarily related to physics.

The knowledge about the experimental setup of Andreas Steffen and Noomen Belmechri made my experiments possible. I want to thank them for spending all the time with me in the lab by which I gained a lot of experimental knowledge. I am grateful to have been given the chance to get to know Dr. Michał Karski. He was one of the persons starting this project.

Dr. Andrea Alberti and Dr. Wolfgang Alt were very helpful with their experienced knowledge in theoretical as well as applied topics. I want to thank them for assisting me with every problem that arose during my Master thesis.

In the end I want to thank my family for their undivided support. Without their help I would have not been able to study physics in this way.

Erklärung der Selbstständigkeit

I hereby certify that the work presented here was accomplished by myself and without the use of illegitimate means or support, and that no sources and tools were used other than those cited.

Bonn, September 26th, 2011 Sebastian Hild